Journal of Computational Physics 228 (2009) 9036–9058

Contents lists available at ScienceDirect

Journal of Computational Physics

journal homepage: www.elsevier.com/locate/jcp

# Adaptive multiscale finite-volume method for nonlinear multiphase transport in heterogeneous formations

S.H. Lee [a,*], H. Zhou [b], H.A. Tchelepi [b]

[a] Chevron Energy Technology Co., 6001 Bollinger Canyon Road, San Ramon, CA 94583-2324, USA
[b] Department of Energy Resources Engineering, Stanford University, Stanford, CA 94305, USA

ARTICLE INFO

*Article history:*
Received 23 December 2008
Received in revised form 10 July 2009
Accepted 8 September 2009
Available online 17 September 2009

*Keywords:*
Multiscale finite-volume
Adaptivity
Multigrid
Multiphase flow
Nonlinear transport
Porous media
Reservoir simulation

ABSTRACT

In the previous multiscale finite-volume (MSFV) method, an efficient and accurate multiscale approach was proposed to solve the elliptic flow equation. The reconstructed fine-scale velocity field was then used to solve the nonlinear hyperbolic transport equation for the fine-scale saturations using an overlapping Schwarz scheme. A coarse-scale system for the transport equations was not derived because of the hyperbolic character of the governing equations and intricate nonlinear interactions between the saturation field and the underlying heterogeneous permeability distribution. In this paper, we describe a sequential implicit multiscale finite-volume framework for coupled flow and transport with general prolongation and restriction operations for both pressure and saturation, in which three adaptive prolongation operators for the saturation are used. In regions with rapid pressure and saturation changes, the original approach, with full reconstruction of the velocity field and overlapping Schwarz, is used to compute the saturations. In regions where the temporal changes in velocity or saturation can be represented by asymptotic linear approximations, two additional approximate prolongation operators are proposed. The efficiency and accuracy are evaluated for two-phase incompressible flow in two- and three-dimensional domains. The new adaptive algorithm is tested using various models with homogeneous and heterogeneous permeabilities. It is demonstrated that the multiscale results with the adaptive transport calculation are in excellent agreement with the fine-scale solutions. Furthermore, the adaptive multiscale scheme of flow and transport is much more computationally efficient compared with the previous MSFV method and conventional fine-scale reservoir simulation methods.



## 1. Introduction

Multiscale flow in natural porous media has been extensively investigated from the pore scale (~10 μm) to geological scales; however, translating the physical phenomena and their mathematical representations across scales is not well established and is an active research area. This paper is concerned with the development of an efficient multiscale algorithm that can be used to simulate flow and transport in highly detailed reservoir models. We assume that the Darcy based representation of the physics is valid for the reference fine-scale.

The quality of the predictions obtained from flow simulations depends strongly on the ability of the reservoir model to represent the complex heterogeneity of the properties that control the flow dynamics in natural porous media. The permeability of natural geologic formations displays high variability levels and complex structures of spatial heterogeneity that

* Corresponding author. Tel.: +1 925 842 6392; fax: +1 925 842 6283.
*E-mail addresses:* seon@chevron.com (S.H. Lee), huizhou@stanford.edu (H. Zhou), tchelepi@stanford.edu (H.A. Tchelepi).

0021-9991/$ - see front matter © 2009 Elsevier Inc. All rights reserved.
doi:10.1016/j.jcp.2009.09.009

span a wide range of length scales [9]. As a result, there has been strong emphasis on characterizing the reservoir properties (permeability) in great detail and on developing efficient solution schemes for coupled multiphase flow and transport in geometrically complex and highly heterogeneous reservoir models.

Recent advances in multiscale methods show great promise in simulating complex flow dynamics in strongly heterogeneous domains. Current multiscale methods usually employ two scales. Hou and Wu [14] introduced a multiscale finite-element method as an efficient algorithm to solve elliptic problems. In order to reduce the resonance effect of the boundary conditions, they also devised an over-sampling technique. Later Chen and Hou [7] presented a multiscale formulation based on mixed finite-element methods and demonstrated clearly that a locally conservative scheme is a necessary requirement for accurate simulation of transport problems. Arbogast [2] and Arbogast and Bryant [3] proposed a multiscale mixed finite-element method. To localize the problem, they applied a closure approximation that all the net flux between coarse elements occurs on the coarse scale. Numerical Greens functions were employed to couple the fine-scale influence with the coarse-scale effects. Chen et al. [6] developed a local-global upscaling method for flow in porous media. They used some global information to update the boundary conditions for the local fine-scale problems and reconstructed the fine-scale velocity field to compute the transport.

Jenny et al. [16–18] developed a multiscale finite-volume (MSFV) method for flow, as well as adaptive IMPES (Implicit Pressure, Explicit Saturations) and sequential implicit methods for coupled multiphase flow and transport. The MSFV method solves flow (pressure and total-velocity) and transport (saturations) sequentially. The flow part uses a global pressure solution on a coarse grid and local fine-scale basis functions to reconstruct the fine-scale pressure field. A second set of basis functions is employed to reconstruct a locally conservative fine-scale velocity field. In the transport part, saturations are updated using local fine domains, defined by the imposed primal coarse-grid, in an adaptive manner. The MSFV method is locally conservative with excellent scalability properties. The method has been proved to be accurate for problems that exhibit high levels of permeability variation. Lunati and Jenny [21,22] investigated compressibility and gravity effects in the multiscale finite-volume method. Recently Lee et al. [19] extended MSFV to the black-oil formulation (three-phase flow with compressibility, capillary pressure and gravity) by using operator splitting of the pressure equation.

Existing multiscale approaches for flow in porous media employ local basis functions, which capture the flow dynamics, to construct a coarse-scale pressure equation. Once the global coarse system is solved, the fine-scale pressure field is reconstructed using (possibly different) basis functions. And then the nonlinear hyperbolic (or parabolic) transport equation is directly, or iteratively, solved for the fine-scale saturation field.

Compared with the flow problem (elliptic pressure equation), development of coarse-scale operators for the nonlinear transport problem (saturation equations) is much more challenging. The hyperbolic nature of the transport equation entails prolongation and restriction operators that are strongly dependent on the history and nonlinear evolution of the saturation field and involve complex interactions with the flow field and the underlying heterogeneous permeability distribution. These complexities are particularly important when the correlation length of the permeability is much larger than the coarse-grid size, which is often the case in natural large-scale formations. In the reservoir engineering community, the pseudo-relative permeability approach has been proposed for upscaling multiphase flow in porous media. However, it has been documented quite clearly that pseudo-relative permeabilities depend strongly on the boundary conditions, specific flow scenario, and saturation history (time). As a result, there is growing consensus that the inaccuracy of pseudo-relative permeability functions is too large to be accepted as a viable alternative to fine-grid simulation [4].

Recently, Efendiev and co-workers [11,12] proposed upscaling schemes, in which the sub-scale effects appear as a nonlinear nonlocal term in the coarse-scale saturation equation. Hou et al. [15] derived a mathematical framework for the homogenized equations for the coupled pressure and saturation equations by projecting the fluctuation onto averages along streamlines. They also resolved the limitation of small fluctuations in the quantities. Aarnes and Efendiev [1] recently proposed two algorithms for the coarse-to-fine interpolator for the transport equations. In the local (first) approach, the coarse-grid transport equation is solved with a fixed velocity field and somewhat arbitrary saturation boundary conditions. The fine-scale saturation evolution provides the interpolation operator. In their global (second) approach, the local boundary conditions for the transport equation are updated continuously using the global solution from the previous timestep. Their first algorithm is somewhat similar to the traditional pseudo-relative permeability approach (i.e., multiphase upscaling with a fixed velocity field). The local boundary conditions can be very different from the global solution and can incur significant errors in the interpolation operation. Their second algorithm is more accurate than the first one; but the second algorithm is only slightly less expensive than full simulation on the fine-grid.

Zhou and Tchelepi [24] developed an operator-based algebraic multiscale framework to solve the pressure equation. They show that the MSFV for the elliptic pressure equation [16] can be algebraically represented by prolongation and restriction operators. In this paper, those same operators are used for the pressure equation. Here, we propose adaptive prolongation operations for the transport equation based on the observation that the saturation changes in a coarse cell can be expressed using asymptotic expansions, once the rapidly moving saturation front sweeps through the local region (e.g. Buckley–Leverett saturation front [20]). For regions with relatively slow evolution of the saturation field, linear interpolation operators are constructed and used instead of the overlapping Schwarz method on the primal coarse-grid used by Jenny et al. [18]. We propose a criterion to switch from the Schwartz-overlap method to the linearly interpolated prolongation operators for constructing the saturation field. We propose two approximate prolongation algorithms: (1) a conservative fine-scale algorithm that first interpolates the local velocity field and then updates the fine-scale saturation, and (2) a conservative coarse-scale algorithm that directly interpolates the coarse-scale saturation changes to the fine-scale. The adaptive transport algorithm

described here is designed to obtain an accurate fine-scale solution. In comparison, the purpose of Aarnes and Efendiev [1] is not to get fine-scale details, but rather to introduce a flexible mechanism to model the flow on the coarse scale more correctly. As a result, it is noted that the error norms of the fine-scale saturations in this paper are smaller than those of Aarnes and Efendiev [1].

The paper is organized as follows. In Section 2, we first describe the governing equations for two phase flow and transport. The discrete forms of the flow and transport equations are also derived. In Section 3, a general mathematical framework is presented to describe restriction and prolongation operations that represent the multiscale formulation for both pressure and saturation. In Section 4, we use the prolongation and restriction operators for pressure described by Zhou and Tchelepi [24], and we propose three adaptive prolongation operators for the saturation, depending on the history of saturation development at a given location. In Section 5, we discuss algorithmic issues for this adaptive multiscale finite-volume strategy and summarize the new approach. Numerical examples are presented in Section 6. In the last section, we give some concluding remarks and outline future directions.

## 2. Governing equations and discretized formulation

We study two phase, incompressible flow in a heterogeneous domain $\Omega$,

$$\Phi\frac{\partial S_o}{\partial t}-\frac{\partial}{\partial x_i}\left(k\frac{k_{ro}}{\mu_o}\frac{\partial p}{\partial x_i}\right)=-q_o, \tag{1}$$

$$\Phi\frac{\partial S_w}{\partial t}-\frac{\partial}{\partial x_i}\left(k\frac{k_{rw}}{\mu_w}\frac{\partial p}{\partial x_i}\right)=-q_w, \tag{2}$$

where $p$ is the pressure, $S_\alpha$ are the saturations (the subscript $\alpha$ stands for phase; $o$ for oil and $w$ for water) with $0\leqslant S_\alpha\leqslant 1$ and $S_o+S_w\equiv 1$, $k$ is the heterogeneous permeability, $k_{r_\alpha}$ are the relative permeabilities (which are functions of $S_\alpha$), $\mu_\alpha$ the viscosities and $q_\alpha$ are source terms that represent the wells. Here, $\Phi$ denotes porosity and $t$ time. For the rest of the paper we use $S=S_o$. The permeability $k$ is, in general, given as a tensorial function of spacial position, but for simplicity, $k$ is assumed to be strongly heterogeneous but locally isotropic. We assume that capillary pressure, gravity, and compressibility are negligible. Equivalently, Eqs. (1) and (2) can be rewritten as

$$\nabla\cdot\lambda\nabla p=q_o+q_w, \tag{3}$$

$$\Phi\frac{\partial S}{\partial t}+\nabla\cdot(f_o\mathbf{u})=-q_o, \tag{4}$$

on $\Omega$, and the total-velocity becomes

$$\mathbf{u}=-\lambda\nabla p \tag{5}$$

with the total mobility and oil-phase fractional flow given by

$$\lambda=k(k_o+k_w), \tag{6}$$

$$f_o=\frac{k_o}{k_o+k_w}, \tag{7}$$

where $k_\alpha\equiv k_{r_\alpha}/\mu_\alpha$ for $\alpha\in\{o,w\}$. The permeability heterogeneity is a dominant factor that dictates the flow behavior in natural porous formations. The heterogeneity of permeability $k$ is usually represented as a complex multiscale function of space. Moreover, as $k$ tends to be highly discontinuous, resolving the spatial correlation structures and capturing the variability of permeability requires highly detailed descriptions.

On the boundary $\partial\Omega$, either pressure $p$, or the flux $\mathbf{u}\cdot\mathbf{n}$ is specified, where $\mathbf{n}$ is the unit-normal vector pointing outward. Eqs. (3) and (4) are a representative description of the type of system that must be handled efficiently by a subsurface flow simulator. Note that the ability to handle the limiting case of incompressible flow ensures that compressible systems can also be solved because compressibility tends to make the overall system of equations less stiff.

The discrete form of Eq. (3) for cell $i$ becomes

$$\sum_{j\in\aleph_i}\lambda_{ij}t_{ij}(p_j-p_i)=q_{o,i}+q_{w,i}. \tag{8}$$

Here, $\aleph_i$ denotes the neighboring cells of cell $i$; and $\lambda_{ij}$ and $t_{ij}$ denote the mobility and transmissibility at the interface of cells $i$ and $j$, respectively. The source/sink terms $q_{o,i}$ and $q_{w,i}$ are the integral strength of source/sink of the oil and water phases in cell $i$, respectively. The discretized transport equation becomes

$$\frac{\Phi V_i}{\Delta t}\left(S_i^{n+1}-S_i^n\right)+\sum_{j\in\aleph_i}f_{o,ij}u_{ij}=-q_{o,i}, \tag{9}$$

where $V_i$ denotes the volume of cell $i$ and $\Delta t$ the timestep size. The discrete velocity at the interface of cells $i$ and $j$ is given by

$$u_{ij}=t_{ij}\lambda_{ij}(p_i-p_j). \tag{10}$$

## 3. Restriction and prolongation operators

Zhou and Tchelepi [24] developed an algebraic multiscale framework to solve the pressure equation, where the main idea is to cast the multiscale scheme using algebraic operators, namely, prolongation and restriction. For the MSFV method, the prolongation operator is assembled from the (dual) basis functions and the restriction operator is piecewise constant, which guarantees mass conservation on the coarse scale. Using this algebraic framework, multiscale formulations for the flow problem can be described as special two-level multigrid schemes with specific choices of the prolongation and restriction operators, in which pre- or post-smoothing is not (usually) performed. In this section, we describe a multiscale method using general prolongation and restriction operators for both flow and transport. In the next section, these operators will be described in detail for the MSFV method.

Let us denote the original fine-scale domain as $\Omega^h$ and the coarse-scale domain as $\Omega^H$ with $H \gg h$. The $\Omega^h$ and $\Omega^H$ represent not only the space with grid scale $h$ and $H$, respectively, but also the space of vectors defined on that grid. The linearized pressure equation and the nonlinear saturation equation for $\Omega^h$ can be written as

$$L^h \mathbf{p}^h + \mathbf{q}^h = 0 \quad \text{for } \mathbf{p}^h \in \Omega^h, \tag{11}$$

$$A^h(\mathbf{S}^h) + \mathbf{r}^h = 0 \quad \text{for } \mathbf{S}^h \in \Omega^h. \tag{12}$$

The pressure equation is linear; whereas the saturation equation is a nonlinear equation because of the nonlinear functional dependency of fractional flow on saturations (i.e., the nonlinear operator $A$ in Eq. (12)). The $\mathbf{q}^h$ denotes the source/sink term and $\mathbf{r}^h$ the right hand side of the saturation equation. The nonlinear Eq. (12) will be iteratively solved by Newton's method.

The prolongation operator for pressure is defined by

$$\mathbf{p}^h = I_H^{h,P} \mathbf{p}^H. \tag{13}$$

Then the restriction operator is applied to Eq. (11), and we obtain the following coarse-scale operator:

$$R_h^{H,P} L^h I_H^{h,P} \mathbf{p}^H + R_h^{H,P} \mathbf{q}^h = 0. \tag{14}$$

The coarse-scale operator is thus given by

$$L^{H,P} = R_h^{H,P} L^{h,P} I_H^{h,P}, \tag{15}$$

Eq. (14) can be written in terms of coarse-scale quantities as follows:

$$L^{H,P} \mathbf{p}^H + \mathbf{q}^H = 0 \quad \text{for } \mathbf{p}^H \in \Omega^H. \tag{16}$$

Similarly, we can define the prolongation operator for saturation:

$$\mathbf{S}^h = I_H^{h,S} \mathbf{S}^H. \tag{17}$$

Again, the restriction operator is applied to Eq. (12):

$$R_h^{H,S} A^h (I_H^{h,S} \mathbf{S}^H) + R_h^{H,S} \mathbf{r}^h = 0 \quad \text{for } \mathbf{S}^H \in \Omega^H. \tag{18}$$

Eq. (18) can be rewritten as a coarse-scale operator using $\tau$ as the correction due to the nonlinearity of $A$:

$$A^H(\mathbf{S}^H) + R_h^{H,S} \mathbf{r}^h - \tau_h^H = 0 \quad \text{for } \mathbf{S}^H \in \Omega^H, \tag{19}$$

where $A^H$ is the coarse-scale operator and the correction, $\tau_h^H$ [5], is defined by

$$\tau_h^H = A^H(R_h^{H,S} \mathbf{S}^h) - R_h^{H,S} A^h(\mathbf{S}^h). \tag{20}$$

## 4. Multiscale finite-volume approximation

### 4.1. Restriction and prolongation operators for pressure

A conforming coarse-grid with $N$ nodes and $M$ cells is imposed on the original fine-grid (see Fig. 1). Each coarse cell, $\Omega_i^H$ ($i \in \{1, \ldots, M\}$), is composed of multiple fine cells. A dual coarse-grid, conforming to the fine-grid, is constructed such that each dual coarse cell, $\Omega_j^D$ ($j \in \{1, \ldots, N\}$), contains exactly one node of the coarse-grid in its interior. The dual coarse-grid has $M$ nodes, $\mathbf{x}_i$ ($i \in \{1, \ldots, M\}$), each in the interior of a coarse cell $\Omega_i^D$. Each dual cell has $N_c$ corners (four in two dimensions and eight in three dimensions). A set of dual basis functions, $\Theta_j^i$, is constructed; one for each corner $i$ of each dual coarse cell $\Omega_j^D$.

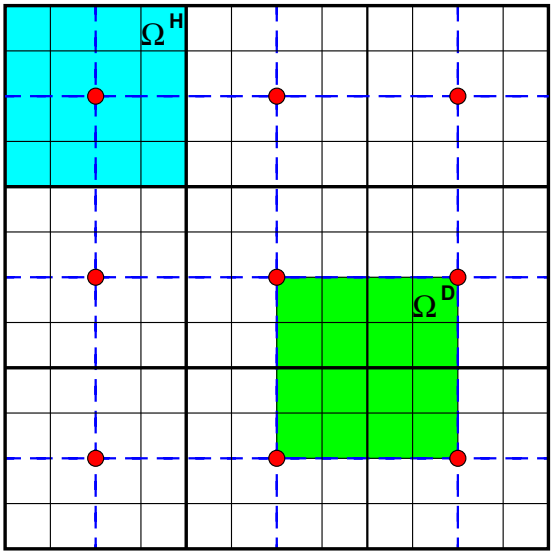


**Fig. 1.** Problem domain partitioned into a primal (solid lines) and dual coarse-grid (dashed line).

Numerical basis functions are constructed for the dual coarse-grid ($\Omega^D$) in Fig. 1. Four dual basis functions, $\Theta^i$ ($i = 1,4$) (8 basis functions for 3-d) are constructed for each dual coarse cell by solving the elliptic problem

$$\nabla \cdot \left(\lambda \nabla \Theta_j^i\right) = 0 \quad \text{on } \Omega_j^D \tag{21}$$

with the boundary condition

$$\frac{\partial}{\partial x_t}\left(\lambda \cdot \nabla \Theta_j^i\right)_t = 0 \quad \text{on } \partial\Omega_j^D, \tag{22}$$

where $x_t$ is the coordinate tangent to the boundary of $\Omega_j^D$. The value at the node $\mathbf{x_k}$ in $\Omega_j^D$ is given by

$$\Theta_j^i(\mathbf{x}_k) = \delta_{ik} \tag{23}$$

where $\delta_{ik}$ is the Kronecker delta. By definition $\Theta_j^i(\mathbf{x}) \equiv 0$ for $\mathbf{x} \notin \Omega_j^D$.

Once the basis functions are computed, the prolongation operator ($I_H^{h,P}$) can be expressed as

$$p_j^h(\mathbf{x}) = I_H^{h,P}\mathbf{p}^H = \sum_i \Theta_j^i p_i^H, \quad \text{for } \mathbf{x} \in \ \Omega_j^D, \tag{24}$$

where the fine-scale pressure is $p_j^h \in \Omega^h$, and the coarse-scale pressure is $p_i^H \in \Omega^H$. The prolongation operator ($I_H^{h,P}$) is a linear combination of the dual basis functions.

Zhou and Tchelepi [24] showed that to ensure mass conservation on the coarse scale, the restriction operator for the finite-volume method takes the form

$$R_h^{H,P} = \begin{cases} 1 & \text{if } \Omega^h \subset \Omega^H, \\ 0 & \text{otherwise.} \end{cases} \tag{25}$$

This restriction operator is simply the sum of the fine-scale conservation equations within a primal coarse cell. Other forms of the restriction operator can be used, i.e., a Galerkin type of restriction operator would be

$$R_h^{H,P} = \left(I_H^{h,P}\right)^T. \tag{26}$$

The coarse-scale operator is then naturally constructed from Eq. (15). Zhou and Tchelepi [24] showed that when the finite-volume type of restriction operator as in Eq. (25) is used, the resulting coarse-scale system is exactly the same as that of the multiscale finite-volume method [16].

The coarse-scale pressure, $\mathbf{p}^H$, is then obtained by solving the global coarse-scale system Eq. (16); the fine-scale pressure is then reconstructed linearly using the prolongation operator of Eq. (24).

### 4.2. Restriction and prolongation operators for saturation

For saturation, we use the conservative restriction operator used for pressure, namely,

$$R_h^{H,S} = R_h^{H,P}. \tag{27}$$

To maintain mass conservation on the coarse and fine-scales, the coarse-scale saturation is naturally defined as the volume average saturation for each primal coarse cell:

$$S_i^H = \frac{1}{V_i} \sum_{\ell \in \Omega_i^H} v_\ell S_\ell^h, \tag{28}$$

where $v_\ell$ is the volume of fine cell $\ell$, and $V_i$ is the volume of coarse cell $i$. If the fine-scale total-velocity is given, the nonlinear fine-scale saturation operator can be written as

$$A_i^h(\mathbf{S}^h) = \sum_{j \in \aleph_i} \frac{k_o\left(S_{o,ij}^h\right)}{k_o\left(S_{o,ij}^h\right) + k_w\left(S_{w,ij}^h\right)} u_{ij} - \beta_i\left(S_i^{h,n+1} - S_i^{h,n}\right). \tag{29}$$

Here,

$$\beta_i = \frac{\Phi V_i}{\Delta t}. \tag{30}$$

The $S_{,ij}$ and $u_{ij}$ denote the upwind saturation and the total-velocity between cells $i$ and $j$, respectively. Furthermore, the coarse-scale total-velocity and fractional flow are defined as:

$$U_{ij}^H = \sum_{\ell \in \partial\Omega_{ij}^H} u_\ell^h, \tag{31}$$

$$F_{ij}^H = \frac{1}{U_{ij}^H} \sum_{\ell \in \partial\Omega_{ij}^H} f(S_\ell^h) u_\ell^h. \tag{32}$$

There are two main difficulties in constructing multiscale solutions for saturation compared with those for pressure. First, it is practically impossible to construct basis functions for saturation by solving local problems, as we do for pressure. With the propagation of the saturation field, the local saturation distribution changes dramatically as a function of time. Therefore, it is quite hard to define a general prolongation operator for saturation. The other difficulty is that the fractional flow curve $f\left(S_\ell^h\right)$ is a strongly nonlinear function of saturation (i.e., $S$-shaped), and in addition, multiphase flow effects interact with the underlying heterogeneous permeability field in a complex manner. The coarse-scale fractional flow $F_{ij}^H$ is, in general, a nonlinear function that cannot be presented solely as a function of the coarse-scale saturation, $\mathbf{S}^H$. As a result, the coarse-scale saturation operator cannot be derived directly using simple restriction and prolongation operators.

In a displacement process, the injected fluid moves from an injection well toward a production well, in which a Buckley–Leverett-like saturation distribution will be established with complex interactions of the saturation front with the underlying heterogeneity in permeability. Typical saturation profiles at times $t$ and $t + \Delta t$ for a 1D problem are shown in Fig. 2.

The Buckley–Leverett profile motivates the design of an adaptive algorithm in which, for the time interval of interest, the domain is divided into three regions: (1) Region 1 where the injection fluid has not reached, (2) Region 2 where an injection front encroached and the saturation of the injection fluid increases rapidly, and (3) Region 3 where the saturation distribution in the fine-scale cells contained in a given coarse cell is mostly established after the sharp front has moved through. The

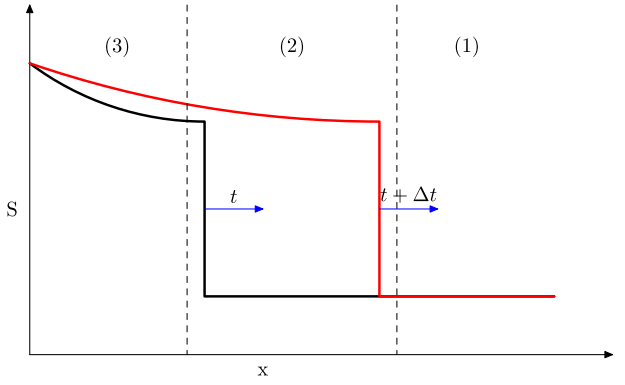


**Fig. 2.** Typical Buckley–Leverett saturation profiles at time $t$ and $t + \Delta t$ for a 1D problem.

saturation change is slow in the expansion fan of the Buckley–Leverett profile [20]. Therefore, the idea is to construct an approximate coarse-scale saturation solution that can be used to decompose the domain into three regions for the time interval of interest. Then different prolongation operators are defined and used adaptively in the different regions.

If the saturation in a coarse cell increases, or decreases, monotonically after the saturation front has moved through, we can estimate the coarse-scale fractional flow curve from the saturation changes of the previous time step, or iteration. Let us express the saturation change in a fine cell as a fraction of the coarse-grid saturation change as

$$\xi_\ell = \frac{\delta S_\ell^h}{\delta S_i^H} \quad \text{for } \ell \in \Omega_i^H. \tag{33}$$

The fractional flow curve can be linearized as

$$f\left(S_\ell^h + \delta S_\ell^h\right) \simeq f\left(S_\ell^h\right) + \frac{\partial f}{\partial S_\ell^h}\xi_\ell \delta S_i^H, \tag{34}$$

$$F_{ij}^H\left(S_i^H + \delta S_i^H\right) \simeq F_{ij}^H\left(S_i^H\right) + \frac{\delta S_i^H}{U_{ij}^H}\sum_{\ell\in\partial\Omega_{ij}^H}\frac{\partial f}{\partial S_\ell^h}\xi_\ell u_\ell^h. \tag{35}$$

With the coarse-scale fractional flow, the coarse-scale nonlinear operator can be written as

$$A_i^H(\mathbf{S}^H) - \tau_h^H \approx \sum_{j\in\aleph_i^H} U_{ij}^H F_{ij}^H - \beta_i\left(S_i^{H,n+1} - S_i^{H,n}\right). \tag{36}$$

Here, $\aleph_i^H$ denotes the neighboring coarse-scale cells to coarse cell $i$.

The coarse-scale saturation, $S^H$, is obtained from Eq. (19) with Eq. (36); and as shown in Section 5.4 the three computational regions can be identified based on changes in the coarse-grid saturation and velocity. We now show how to adaptively construct the fine-grid saturation field in the three regions using the various prolongation operators.

#### 4.2.1. Prolongation Operator I

When the invading fluid moves into a coarse cell, sharp saturation changes accompanied by complex interactions with the underlying heterogeneous permeability take place. In this situation, a conservative velocity field has to be constructed before solving the transport problem. The construction of a conservative velocity field is described briefly here. A detailed discussion can be found in Jenny et al. [16].

In this region with significant changes in saturation as a function of time, we do not have a rigorous prolongation operator that allows us to avoid solving the local fine-scale transport problem. So, the fine-grid solution is computed using a block-based Schwarz overlap method [18]. Because this amounts to full reconstruction, it is an accurate 'prolongation' scheme but computationally expensive. As a result, we employ full-reconstruction adaptively only for regions, in which rapid saturation changes are detected.

We solve Eq. (12) for the domain $\Omega_i^H$

$$A_i^h(\mathbf{S}^{h,v+1}) + \mathbf{r}^{h,v+1} = 0 \quad \text{for } \mathbf{S}^h \in \Omega_i^H \tag{37}$$

with the Neumann boundary conditions:

$$S_\ell^{h,v+1} = S_\ell^{h,v}, \quad u_\ell^{h,v+1} = u_\ell^{h,v} \quad \text{for } \ell \in \partial\Omega_{ij}^H. \tag{38}$$

The superscript $v$ indicates the iteration level and the approximation of Eq. (38) provides the localization of the problem so that the equation can be solved for each coarse cell. From Eq. (28), the coarse-grid saturation can be computed readily from the fine-grid saturation. This first method is locally conservative and accurate in constructing fine-grid saturations; however, it entails several iterative implicit computations of saturations on the primal coarse cells with Neumann boundary conditions to obtain a globally converged solution. Furthermore, this approach also involves an expensive process for constructing a conservative velocity field.

#### 4.2.2. Prolongation Operator II

The second method comprises two steps: (1) reconstruction of a locally conservative fine-grid velocity field using direct interpolation of the coarse-grid velocity and (2) explicit computation of fine-grid saturations. Assume that the velocity distributions at the coarse and fine-grids are available from the previous time step, or the previous iteration $(v)$: $U_i^{H,v}$ for coarse cell $i$ and $u_j^{h,v}$ for fine cell $j \in \Omega_i^H$. From the coarse-grid solution of Eq. (16), we obtain a new coarse-grid velocity: $U_i^{H,v+1}$. If the velocity does not change much, we can interpolate the coarse-grid velocity change to the fine-grid velocity at the new iteration level. For Cartesian grids, the interpolation can be expressed in a simple form:

$$u_j^{h,v+1}(\mathbf{x}) = u_j^{h,v}(\mathbf{x}) + U_i^{H,v+1}(\mathbf{x}_0) - U_i^{H,v}(\mathbf{x}_0) + \frac{\mathbf{x}-\mathbf{x}_0}{\mathbf{x}_1-\mathbf{x}_0}\otimes\left(U_i^{H,v+1}(\mathbf{x}_1) - U_i^{H,v}(\mathbf{x}_1) - U_i^{H,v+1}(\mathbf{x}_0) + U_i^{H,v}(\mathbf{x}_0)\right), \tag{39}$$

where $\mathbf{x}/\mathbf{y} = (x_1/y_1, x_2/y_2)$, $\mathbf{u}\otimes\mathbf{v} = (u_1v_1, u_2v_2)$ and $\mathbf{x}_0$ and $\mathbf{x}_1$ are the coordinates of the coarse grid at the bottom-left and top-right corners, respectively. We can readily prove that if $u_j^{h,v}$ and $U^{H,v+1}$ are conservative on the fine and coarse grids,

respectively, the interpolated fine-grid velocity, $u_j^{h,v+1}$, is also conservative on the fine-grid. Once the fine-grid velocity is estimated, the saturation can be inexpensively computed using an explicit method:

$$S_j^{h,v+1} = S_j^{h,v} + \frac{\Delta t}{v_j} \sum_\ell u_\ell^{h,v+1} f(S_j^{h,v}). \tag{40}$$

The stability of the explicit saturation calculation will be governed by the CFL number:

$$\mathrm{CFL} = u_j \frac{\partial f\left(S_j^h\right)}{\partial S_j^h} \frac{\Delta t}{\Delta x}. \tag{41}$$

The CFL number should be less than one for stability of the explicit calculation [20]. If this algorithm is applied in the domain where $\partial f\left(S_j^h\right)/\partial S_j^h \ll 1$ (i.e., rarefraction behind the Buckley–Leverett front), the timestep size restriction will be small. If there is a timestep size restriction due to stability, we can use local time stepping, or an implicit formulation:

$$S_j^{h,v+1} = S_j^{h,v} + \frac{\Delta t}{v_j} \sum_\ell u_\ell^{h,v+1} f\left(S_j^{h,v+1}\right). \tag{42}$$

#### 4.2.3. Prolongation Operator III

We now devise a fast interpolation of saturation that is locally conservative on the coarse-grid. If the saturation distribution pattern does not change much between iterations, or timesteps, we can compute the fine-grid saturation from the coarse-grid saturation change as follows:

$$S_\ell^{h,v+1} = S_\ell^{h,v} + \xi_l \delta S_i^H. \tag{43}$$

Here, we assume that the relative saturation change $(\xi_l)$ does not vary much from the previous iteration. It is a reasonable approximation for a coarse cell, in which the saturation changes are slow behind a steep saturation front. Clearly the accuracy of this interpolator depends on the assumption that $\xi_l$ does not vary much from the previous iteration. As will be shown in the numerical examples, we can identify regions, where this simple interpolator can be safely applied to yield high numerical efficiency and accuracy. Note that the above prolongation operator does not guarantee saturation conservation on the fine-grid; however, the saturation field is conservative on the coarse grid. Nevertheless, the conservation errors are expected to remain small and bounded because (1) the saturation field is conservative on the coarse-grid, and (2) this prolongation operator is applied only in regions where the saturation changes slowly during the time interval of interest.

## 5. Algorithmic issues and summary

### 5.1. Fine-scale pressure for conservative velocity field

Jenny et al. [16,17] observed that the fine-grid velocity constructed by the coarse pressure $p_i^H$ and the dual basis functions $\Theta_j^i$ yields local mass balance errors near the interfaces between coarse dual cells. They proposed a second set of basis functions to construct a locally conservative fine-scale velocity field. Using the fine-scale fluxes obtained from the dual basis functions as boundary conditions when computing the fine-scale basis functions is crucial for ensuring that the reconstructed fine-scale velocity field is indeed conservative. The fine-scale fluxes, $F$, across a coarse cell are extracted from the interior of dual volumes. The fine-scale basis functions (27 for 3-d and 9 for 2-d) were constructed by solving the pressure equation with the boundary fluxes that were calculated from the dual basis functions for each node. There are two numerical difficulties in this second basis function approach: first the computational cost is large because of the large number of second basis function (27 for 3-d) and secondly the basis function method is limited to a linear system where the superposition principle can be applied. Even though an adaptive method can be employed to eliminate unnecessary computation of the second set of basis functions, the large number of basis functions may not be much more efficient than a direct method for computing the velocity and saturation fields for every time step, or iteration. Furthermore, a direct fine-scale simulation approach does not require strict linearity of the governing equations and can be easily extended to include many nonlinear effects, such as compressibility, capillary pressure, relative permeability, etc. [19].

From the coarse-scale pressure solution and the dual basis functions, we can construct the fine-grid pressure field in a primal coarse cell, $\Omega^H$, as shown in Fig. 1. We apply the Neumann boundary conditions along the primal coarse-grid, $\partial\Omega^H$:

$$\mathbf{u}' = \mathbf{u}_o' + \mathbf{u}_w' = -\lambda_o \cdot \nabla p - \lambda_w \cdot \nabla p \tag{44}$$

and solve Eq. (3) for the fine-scale velocity. In order to obtain a conservative velocity field $\mathbf{u}$ which conforms to $\mathbf{u}'$, the requirement:

$$\mathbf{u} \cdot \mathbf{n} = \mathbf{u}' \cdot \mathbf{n} \tag{45}$$

is imposed at the interfaces between coarse cells, where $\mathbf{n}$ is the interface unit-normal vector. The local fine-scale solution is the solution of Eq. (3) with the local boundary conditions of Eq. (45) and the local pressure solution is readily converted to

velocities. Note that when using Prolongation Operators II and III for the saturation transport equation, the fine-scale velocity is either linearly constructed, or not computed at all. Thus significant gains in computational efficiency can be achieved by using these operators.

### 5.2. Sequential implicit scheme

Jenny et al. [18] proposed a sequential fully implicit MSFV algorithm to solve problems of coupled multiphase flow and transport. Each timestep consists of a Newton loop, and the multiphase flow problem is solved iteratively in two stages. First in each Newton loop, the pressure equation is solved and the velocity field is constructed from the pressure solution as outlined in the previous subsection and explained in detail by Jenny et al. [17,18] and Tchelepi et al. [23]. Then, the transport equation is solved on the fine-grid by using the reconstructed fine-scale velocity field **u**. Using a Schwarz-overlap method, the transport problem is solved locally on each coarse cell using an implicit phase-based upwinding scheme. The saturations from the neighboring coarse cells at the previous iteration level are used as boundary conditions. Once the transport equation is converged, the new saturation distribution determines the total-mobility field for the elliptic problem of the next Newton iteration. The sequential implicit MSFV method has been tested for highly detailed and stiff problems, and the computational experience indicates that the coupling scheme is quite robust even for aggressive time stepping. Here, we employ the sequential fully implicit algorithm of Jenny et al. [18]. However, we adaptively construct the fine-sale fields for pressure, velocity, and saturation as described in the previous section. This adaptive multiscale approach for both flow and transport allows us to achieve high computational efficiency without compromising solution accuracy or numerical stability.

### 5.3. Adaptive scheme for pressure

The most expensive part of the implicit MSFV algorithm for multiphase flow is the reconstruction of the dual basis functions, which serve as the prolongation operator for the pressure equation. Therefore, to obtain a high efficiency, it is desirable to recompute these basis functions only when and where it is absolutely necessary. Jenny et al. [17] developed an adaptive scheme to update these basis functions, in which if the condition

$$\frac{1}{1+\epsilon_\lambda} < \frac{\lambda^\nu}{\lambda^o} < 1+\epsilon_\lambda \tag{46}$$

is not fulfilled for all the fine cells inside a coarse dual cell, then the dual basis functions associated with the coarse cell must be reconstructed. Here, $\lambda^o$ denotes the total-mobility when the basis functions were last updated and $\lambda^\nu$ denotes the total-mobility at the current iteration. The $\epsilon_\lambda$ $(>0)$ is a user defined value. Note that condition (46) is true, if $\lambda$ changes by a factor that is larger than $1/(1+\epsilon_\lambda)$ and smaller than $(1+\epsilon_\lambda)$. Of course, these numbers depend on the user defined threshold $\epsilon_\lambda$. In general, a smaller threshold triggers more fine cells, and as a consequence more basis functions are recomputed each time step. For a wide variety of test cases, Jenny et al. [17] found that taking $\epsilon_\lambda$ to be <0.2 yields marginal changes in the obtained results, and that the fraction of basis functions need to be reconstructed is quite small. In all the numerical examples in this paper, we use $\epsilon_\lambda = 0.2$ for updating the dual basis functions.

### 5.4. Adaptive scheme for saturation

As discussed in Section 4.2, we do not need to compute the fine-scale saturation in Region 1 because there the change in the saturation field over the time interval of interest is negligible. On the other hand, Region 2 entails the most rigorous (and costly) algorithm, Prolongation Operator I, which does not require information regarding the saturation history. In Region 3, an approximate linear interpolator, Prolongation Operators II or III, is used. Prolongation Operator II is more expensive than

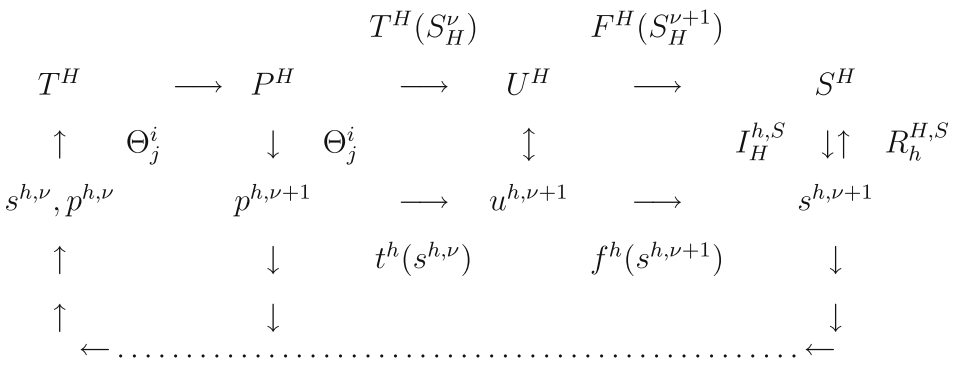


**Fig. 3.** A schematic diagram of the prolongation and restriction operators.

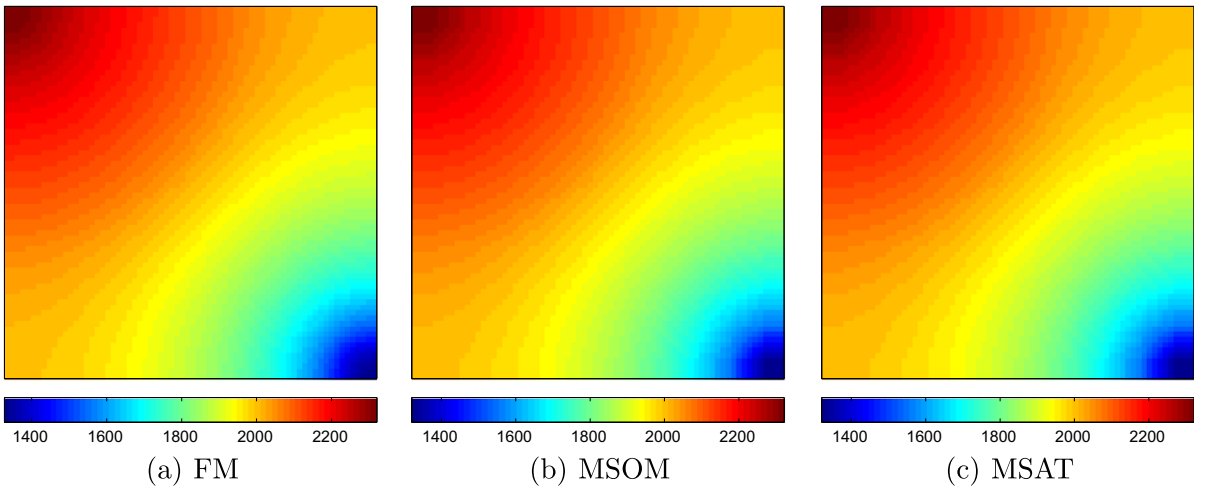


**Fig. 4.** Pressure distribution at $t = 0.2$ PVI in Case 1 with homogeneous permeability.

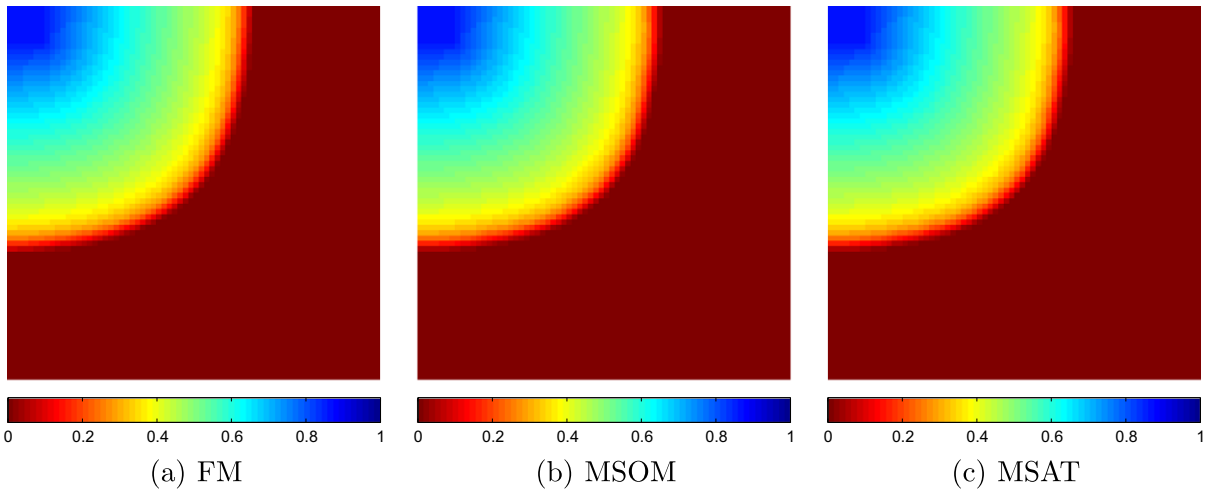


**Fig. 5.** Saturation distribution at $t = 0.2$ PVI for Case 1 with homogeneous permeability.

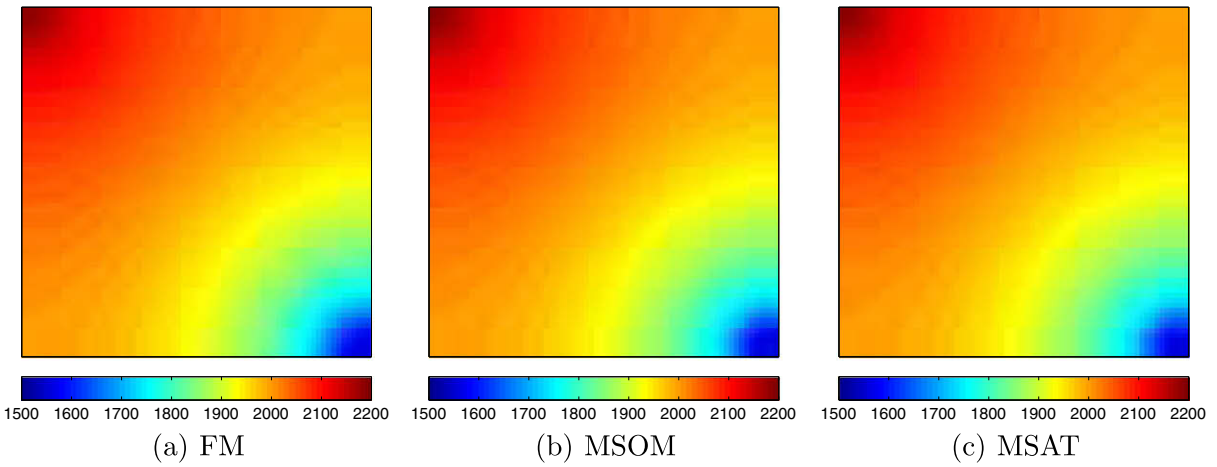


**Fig. 6.** Pressure distribution at $t = 0.8$ PVI for Case 1 with homogeneous permeability.

Prolongation Operator III, but it yields a locally conservative fine-scale saturation, whereas Prolongation Operator III is only locally conservative on the coarse scale. We, thus, need to have a good criterion to use Operator III for Region 3 in order to ensure that the conservation errors on the fine scale are bounded and small.

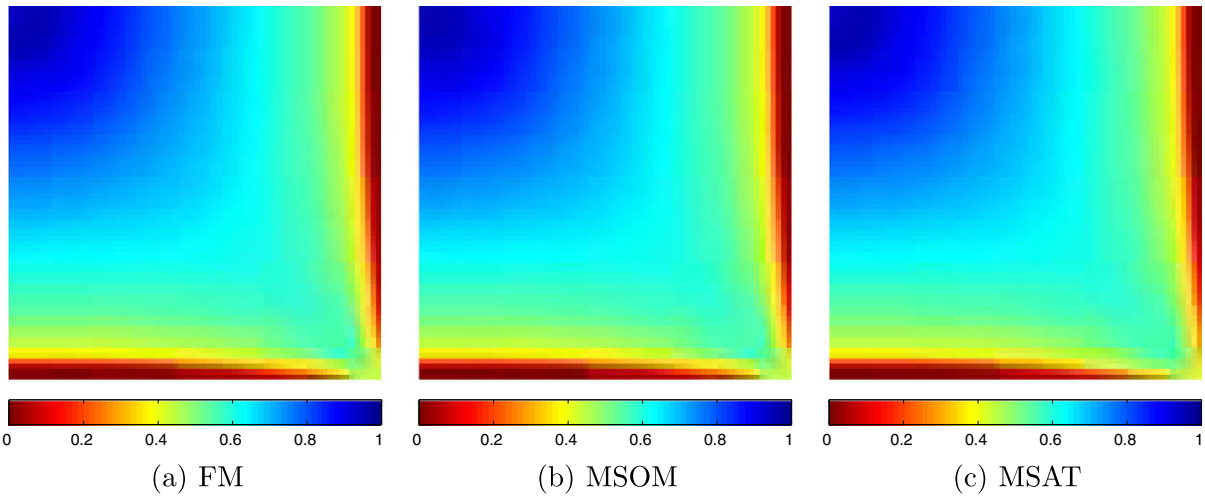


**Fig. 7.** Saturation distribution at $t = 0.8$ PVI for Case 1 with homogeneous permeability.

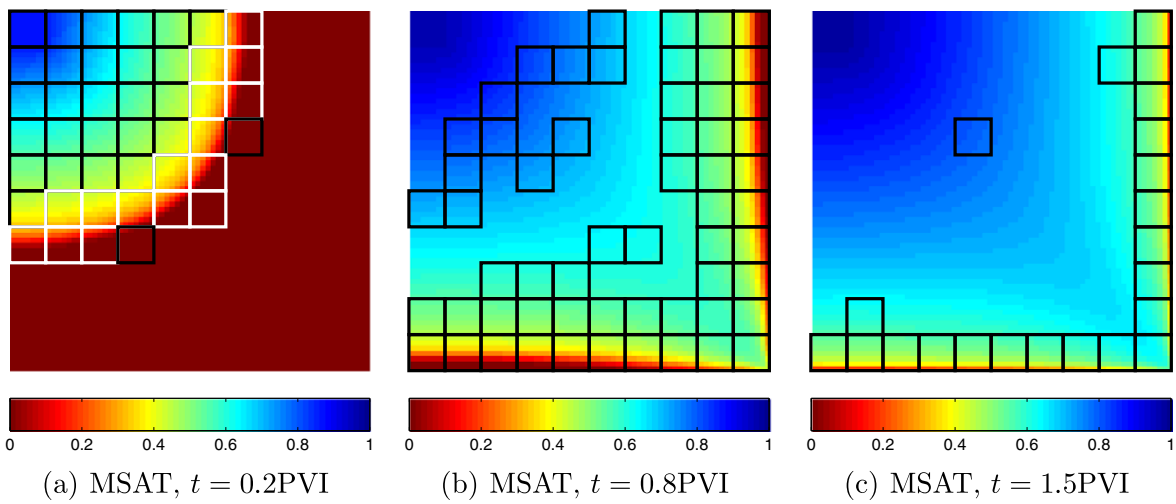


**Fig. 8.** Adaptive saturation computation at three times for Case 1: the white and black squares, respectively, denote the regions where Prolongation Operators I and II are used, at least once, during the iterative saturation computation of the particular time step.

**Table 1**
Error norms and adaptivity statistics for Case 1 with homogeneous permeability: $e_p$ and $e_s$ are $L_2$ error norms for pressure and saturation, respectively. The $f_p$ denotes the fraction of updated pressure basis functions employed from the initial time to the current time step. The $f_{\mathrm{I}}$ and $f_{\mathrm{II}}$, respectively, denote the fraction of Prolongation Operators I and II employed in the transport computations from the initial time to the current time step.

| $t$ (PVI) | $e_p$ | | $e_s$ | | $f_p$ (%) | | $f_{\mathrm{I}}$ (%) | $f_{\mathrm{II}}$ (%) |
|---|---|---|---|---|---|---|---|---|
| | MSOM | MSAT | MSOM | MSAT | MSOM | MSAT | MSAT | MSAT |
| 0.2 | 1.46e−3 | 1.46e-3 | 3.54e−3 | 3.54e−3 | 3.31 | 3.88 | 10.67 | 4.55 |
| 0.6 | 1.24e−3 | 1.07e−3 | 3.03e−3 | 5.43e−3 | 2.89 | 2.85 | 7.56 | 21.42 |
| 0.8 | 1.03e−3 | 8.40e−4 | 2.70e−3 | 6.73e−3 | 2.50 | 2.24 | 6.01 | 26.00 |
| 1.0 | 9.17e−4 | 7.42e−4 | 2.36e−3 | 8.68e−3 | 2.17 | 2.16 | 4.85 | 25.38 |
| 1.2 | 8.40e−4 | 6.94e−4 | 2.14e−3 | 1.04e−2 | 2.05 | 2.06 | 4.15 | 24.15 |
| 1.5 | 7.70e−4 | 6.69e−4 | 1.90e−3 | 1.31e−2 | 1.95 | 1.95 | 3.44 | 22.13 |

To identify the transitions between Regions 1, 2 and 3, we employ criteria based on changes in the coarse-scale velocity and saturation fields, which are readily available from the coarse-scale solutions of pressure (Eq. (16)) and saturation (Eq. (19)). The transition from Region 1 to 2 in coarse cell $i$ is detected using the following simple condition

$$\|\Delta S_i^H\| > \Delta_1, \tag{47}$$

and the transition from Region 2 to 3 is identified by the changes in both saturation and velocity:

$$\|\Delta S_i^H\| < \Delta_2 \quad \text{and} \quad \left( \left\| \frac{\Delta U_i^H}{U_i^H} \right\| < \Delta_v^1 \ \text{for} \ \left\| U_i^H \right\| > \epsilon_v \ \text{or} \ \left\| \Delta U_i^H \right\| < \Delta_v^2 \ \text{for} \ \left\| U_i^H \right\| \leqslant \epsilon_v \right). \tag{48}$$

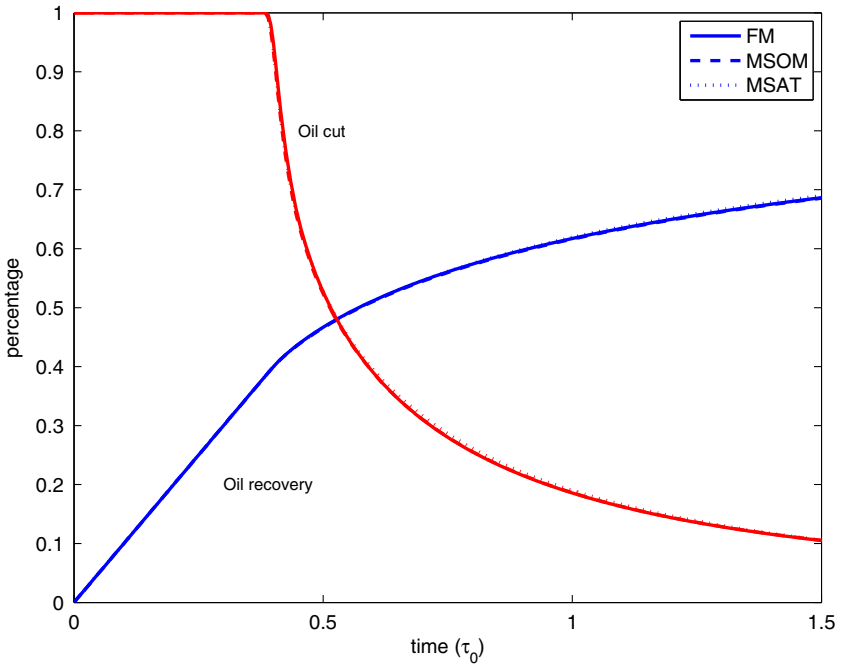


**Fig. 9.** Cumulative oil recovery and oil fraction for Case 1.

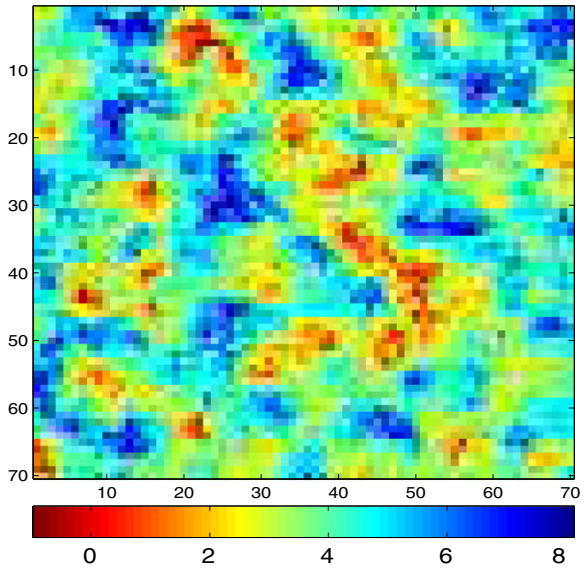


**Fig. 10.** Log-normal permeability field of Case 2.

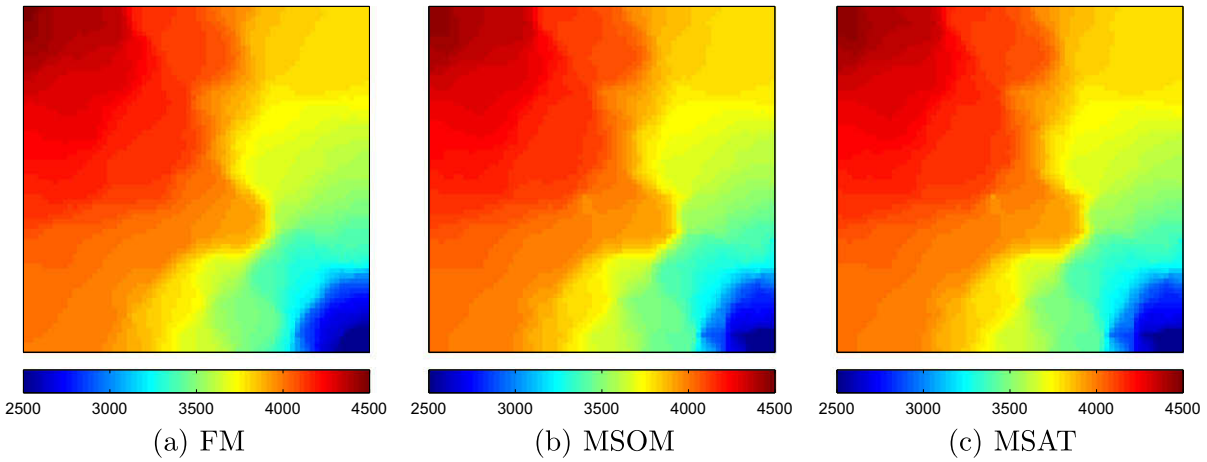


**Fig. 11.** Pressure distribution at $t = 0.2$ PVI in Case 2 with log-normal permeability.

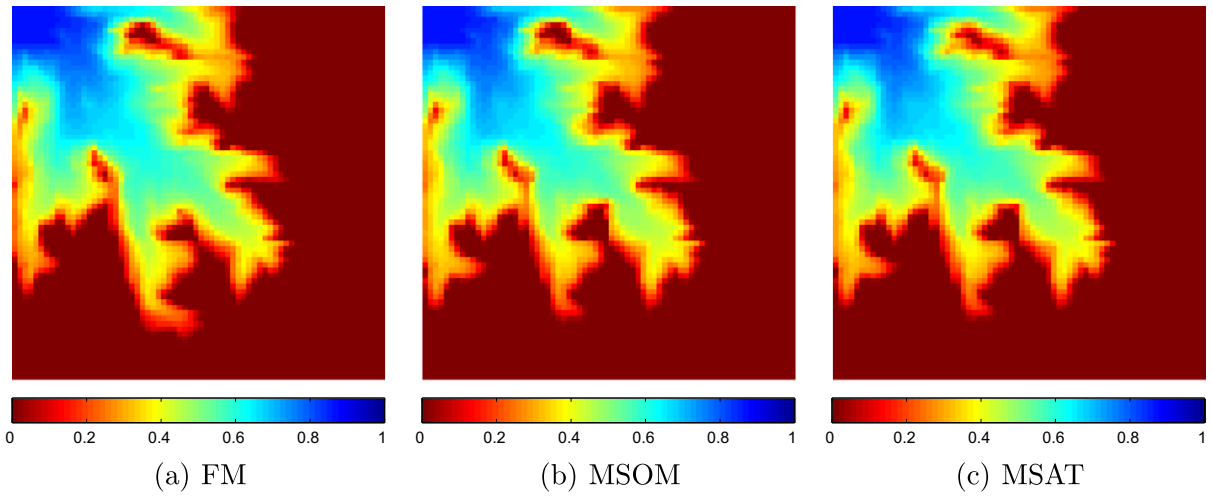


**Fig. 12.** Saturation distribution at $t = 0.2$ PVI in Case 2 with log-normal permeability.

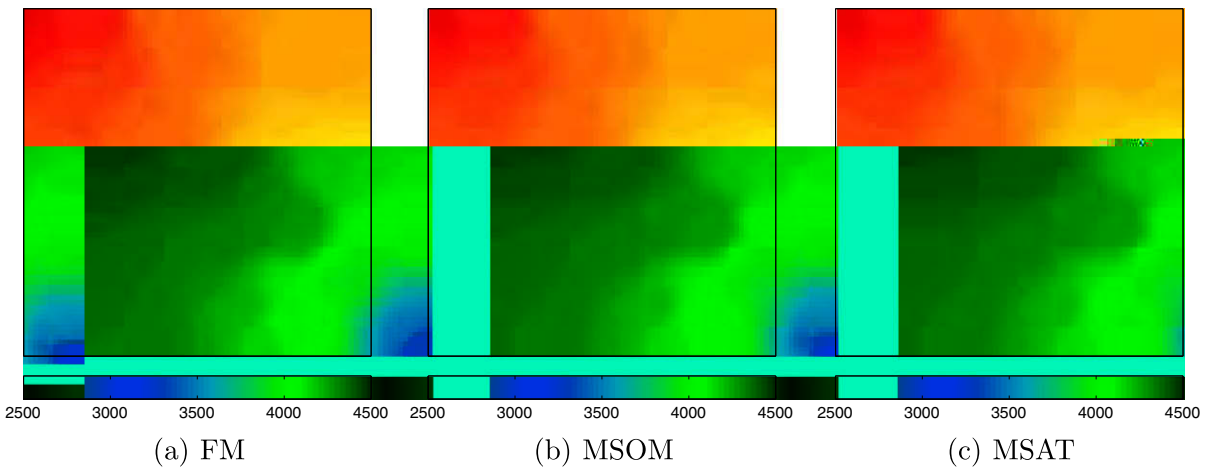


**Fig. 13.** Pressure distribution at $t = 0.8$ PVI in Case 2 with log-normal permeability.

Next, a criterion is needed to choose between Operators II and III for Region 3. If the relative saturation change $\xi_l$ in Eq. (33) dose not vary much, Operator III should yield small fine-scale saturation errors. A variable that gauges the changes in $\xi$ for each coarse cell is introduced:

$$\Xi_i \equiv \frac{\max\{\xi_{l,i}\}}{\min\{\xi_{l,i}\}} \quad \text{for } l \in \Omega_i^H. \tag{49}$$

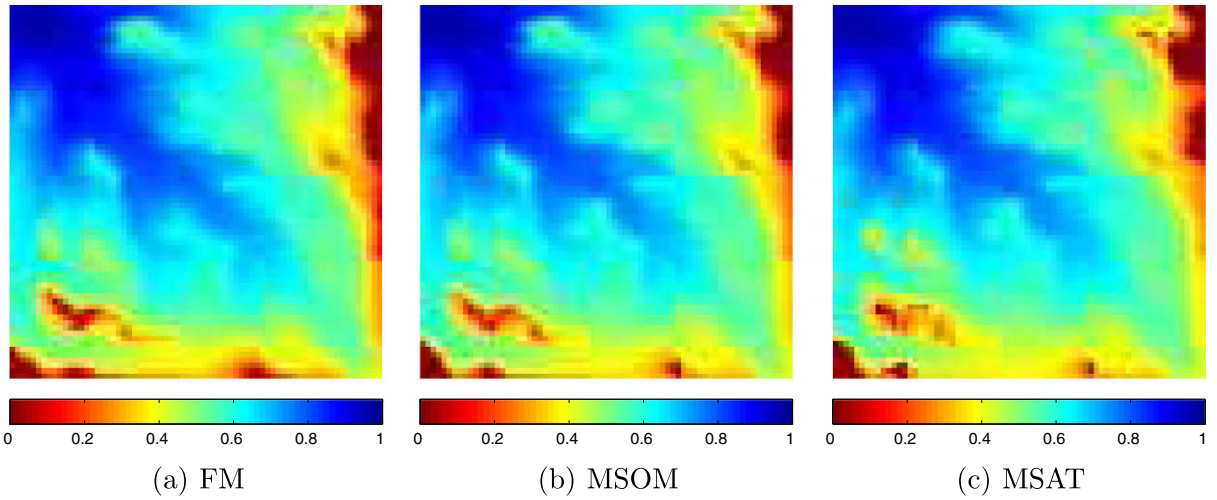


**Fig. 14.** Saturation distribution at $t = 0.8$ PVI in Case 2 with log-normal permeability.

**Table 2**
Error norms and adaptivity statistics for Case 2 with log-normal permeability: the variables are defined in the caption of Table 1.

| $t$ (PVI) | $e_p$ | | $e_s$ | | $f_p$ (%) | | $f_{\mathrm{I}}$ (%) | $f_{\mathrm{II}}$ (%) |
|---|---|---|---|---|---|---|---|---|
| | MSOM | MSAT | MSOM | MSAT | MSOM | MSAT | MSAT | MSAT |
| 0.2 | 1.01e−2 | 9.87e−3 | 3.89e−2 | 3.90e−2 | 2.30 | 2.19 | 7.72 | 5.34 |
| 0.6 | 9.38e−3 | 9.73e−3 | 3.49e−2 | 3.98e−2 | 2.35 | 2.32 | 6.36 | 20.59 |
| 0.8 | 9.10e−3 | 9.66e−3 | 2.99e−2 | 3.96e−2 | 2.11 | 2.10 | 5.23 | 23.69 |
| 1.0 | 8.12e−3 | 8.54e−3 | 2.33e−2 | 3.34e−2 | 1.94 | 1.92 | 4.40 | 23.91 |
| 1.2 | 7.00e−3 | 7.28e−3 | 2.01e−2 | 3.26e−2 | 1.75 | 1.74 | 3.86 | 23.05 |
| 1.5 | 6.15e−3 | 6.31e−3 | 1.90e−2 | 3.29e−2 | 1.55 | 1.54 | 3.29 | 21.49 |

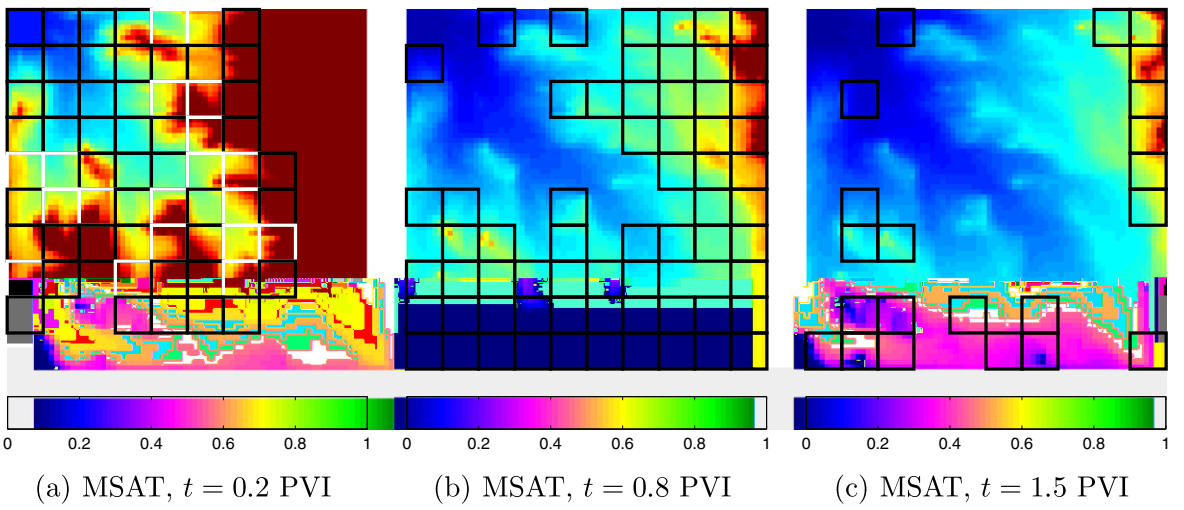


**Fig. 15.** Adaptive saturation computation for three time steps in Case 2: the white and black squares, respectively, denote the region where Prolongation Operator I and II was applied, at least once, in iterative saturation calculation of the time step.

When the condition

$$\Delta\Xi_i < \Delta_\xi \tag{50}$$

is satisfied in Region 3, Operator III is used.

Note that if these criteria become very restrictive, the transport equation will be solved using Prolongation Operator I, which is identical to the original full reconstruction algorithm of Jenny et al. [18]. As the criteria get softer, computational efficiency improves, but the errors are expected to increase. This is a challenging area of ongoing research.

### 5.5. Algorithm summary

A schematic diagram of the prolongation and restriction operators for pressure and saturation is shown in Fig. 3. Hajibeygi et al. [13] recently proposed an iterative MSFV based on this sequential implicit framework. Our adaptive MSFV algorithm can be summarized as follow:

A. Impose primal and dual coarse-grids; construct the restriction operators for pressure and saturation from Eqs. (25) and (27).
B. Pressure Solution
   (1) Derive the basis functions ($\Theta$) from Eq. (21) and local boundary conditions Eqs. (22) and (23).
   (2) Assemble the prolongation operator for pressure from Eq. (24).
   (3) Construct the coarse-grid pressure equation from Eqs. (15) and (16), and then solve for the coarse-grid pressure $\mathbf{p}^H$.
   (4) Construct fine-scale pressure in Eq. (24), $\mathbf{p}^h$, from the coarse pressure $\mathbf{p}^H$ and the basis functions.

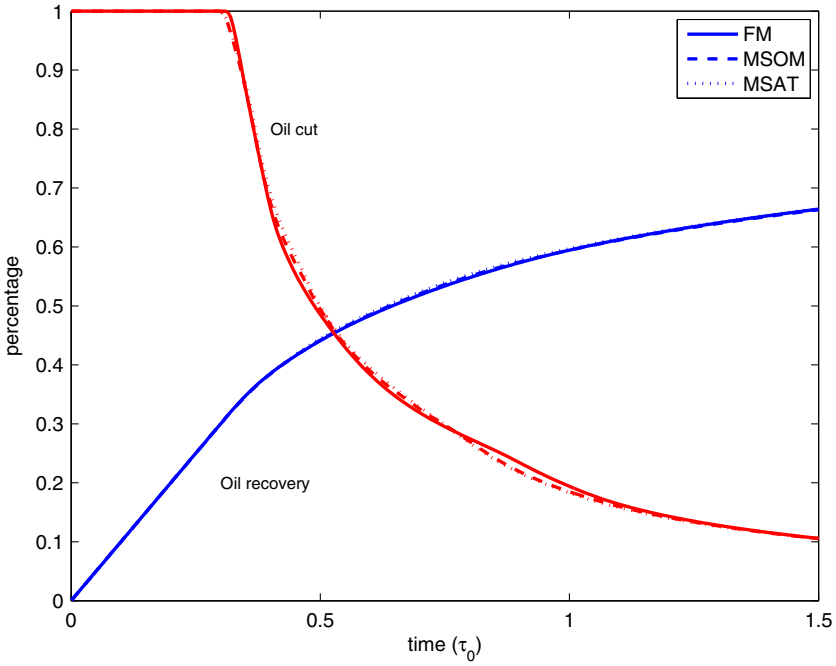


**Fig. 16.** Cumulative oil recovery and oil fraction in production (oil cut) in Case 2.

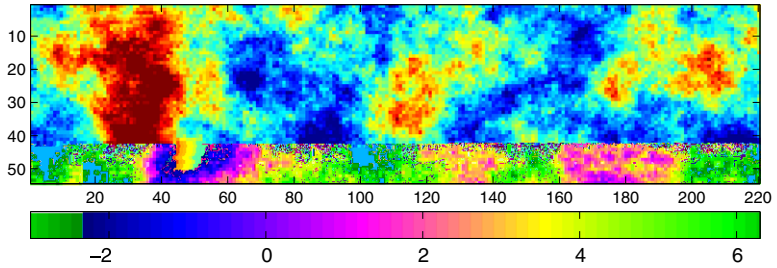


**Fig. 17.** The permeability field extracted from the top layer of SPE10 permeability model.

C. Saturation Solution
   (1) Compute coarse-grid saturations from Eqs. (19) and (36).
   (2) Based on coarse-grid velocity and saturation changes, identify Regions 1,2,and 3, using the criteria, Eqs. (47) and (48). Further, the criterion Eq. (50) is applied to decide the interpolation algorithm for velocity or saturation in Region 3.
   (3) The reconstruction of $\mathbf{p}^h$ can be omitted for Regions 1 and 3.
   (4) For Region 2, construct the Neumann boundary conditions for the primal dual grid from the fine-scale pressure solution, $\mathbf{p}^h(\mathbf{x})$, as described in 5.1. The pressure solution will yield a conservative fine-scale phase velocity, $\mathbf{u}^h$.
   (5) With the computed phase velocities on fine-scale, the phase transport equation are solved for Region 2 and Region 3 with $\Delta\Xi_i \geqslant \Delta_\xi$. Here, an explicit or implicit discretization scheme can be used.
   (6) If the saturation changes in a coarse-grid is in the linear asymptotic domain (Region 3 with $\Delta\Xi_i < \Delta_\xi$), the transport equation for the coarse-grid is solved only for the coarse-grid saturation and the fine-grid saturation will be linearly interpolated, if necessary.

D. Using the new saturation distribution, the total-mobility field $\lambda$ is updated and the basis functions are recomputed where necessary (which includes updating the effective coarse-scale transmissibilities). Here, an adaptive scheme is applied.
E. If an implicit solution method is applied, one proceeds with the next Newton Raphson iteration by repeating steps B through D until convergence is achieved.
F. The next time step is performed by updating variables and repeating steps B through E.

## 6. Numerical examples

Reservoir models with various boundary conditions (source/sink or Dirichlet boundary conditions) are employed in order to test the proposed adaptive algorithm for both pressure and saturation. We studied two-phase flow in four reservoir models: (1) a homogeneous reservoir, (2) a heterogeneous reservoir model with a moderate isotropic permeability correlation length, (3) a highly heterogeneous media with relatively large anisotropic permeability correlation lengths and (4)

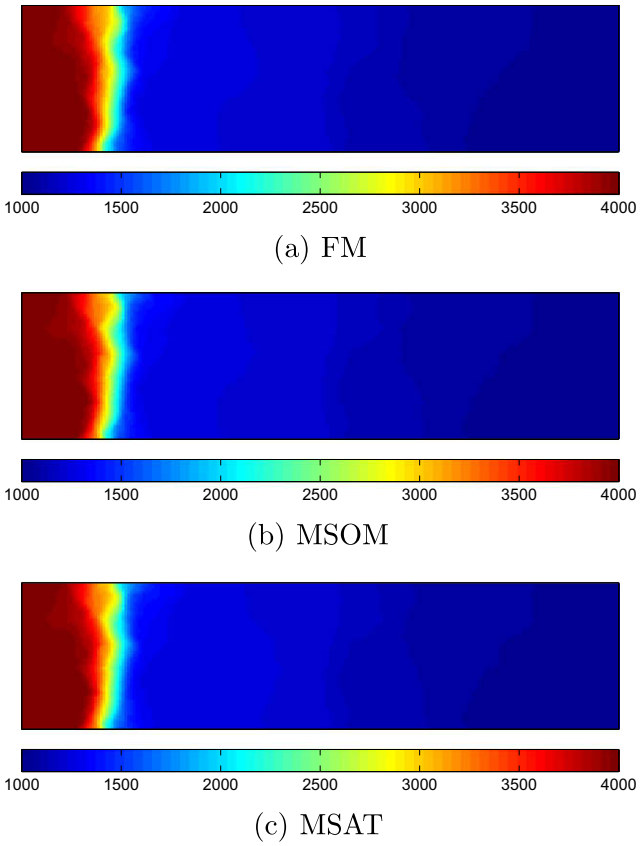


**Fig. 18.** Pressure distribution at $t = \tau_o$ in Case 3 with Dirichlet boundary condition.

three-dimensional, heterogeneous models with different grid numbers. The last example was chosen to demonstrate the numerical efficiency gain by the adaptive transport algorithm. The numerical examples, except the third one, included one injector and one producer at opposite corners of the model. The third example involved a linear displacement process with constant pressure conditions at the inlet and outlet boundaries

The fluids are assumed to be incompressible and the quadratic relative permeability model is employed ($k_{ro} = S_o^2$ and $k_{rw} = S_w^2$). The viscosity ratio between the water and oil is 1:5 (unfavorable displacement). The nonlinear convergence tolerances for pressure and saturation are 1 psi and $10^{-4}$, respectively. In the adaptive transport algorithm, the transition criteria, $\Delta_1 = 10^{-5}$ are chosen for the transition from Region 1 (before the invasion of the injection fluid) to Region 2 (a sharp saturation change due to encroachment of the injection fluid); and $\Delta_2 = 10^{-2}, \Delta_v^1 = 0.1, \Delta_v^2 = 10^{-4}$, and $\epsilon_v = 10^{-4}$ are used for the transition from Regions 2 to 3 (slow saturation change after the saturation front has moved through). Slightly different thresholds of relative saturation change ($\Delta_\xi$) are used in different reservoir models. We found that a highly heterogeneous model requires a tight tolerance of $\Delta_\xi$ in order to maintain numerical accuracy: i.e., $\Delta_\xi = 10^{-3}$ for the first two examples and $\Delta_\xi = 10^{-4}$ for the 10th SPE Comparative Model.

We take the fine-scale solution as reference, and the $L_2$ norms of pressure and saturation errors are defined by

$$e_p = \frac{\|p^{ms} - p^f\|_2}{\|p^{init}\|}, \tag{51}$$

$$e_s = \|S^{ms} - S^f\|_2. \tag{52}$$

Note that the pressure error norm $e_p$ is normalized by the initial pressure in Cases 1 and 2, but in the linear displacement process of Case 3, we employ the pressure difference between the inlet and outlet boundaries to normalize $e_p$.

### 6.1. Case 1: Homogeneous domain

We now consider a two-dimensional reservoir model of 700 ft $\times$ 700 ft with homogeneous permeability $k = 100$ md. Even though the domain is two-dimensional, the model is assumed to have a unit thickness (1 ft) in the third direction for the convenience in specifying the operating conditions. The fine-scale grid, $70 \times 70$, is uniformly coarsened into a

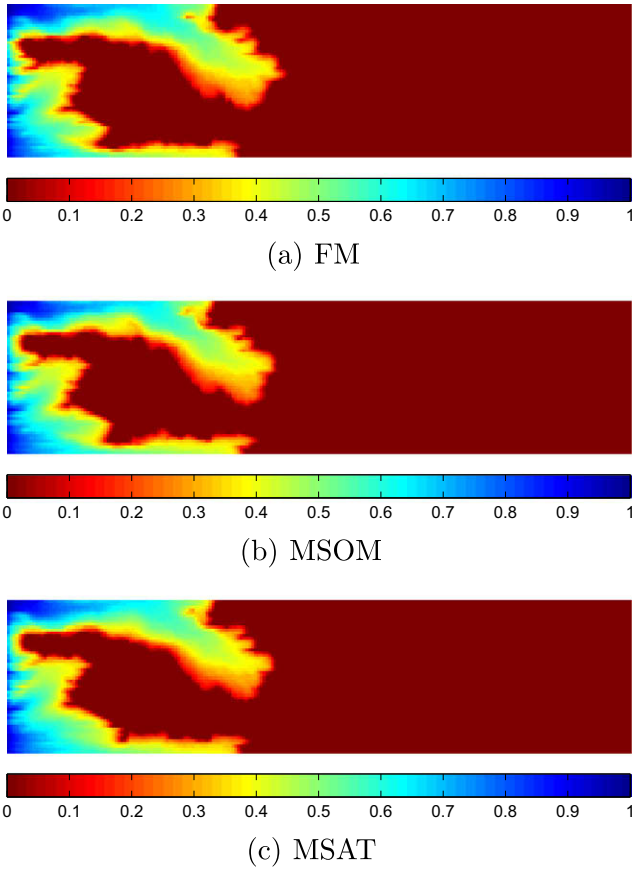


**Fig. 19.** Saturation distribution at $t = \tau_o$ in Case 3 with Dirichlet boundary condition.

$10 \times 10$ coarse-grid. The upscaling factor is 49 as each coarse block comprises $7 \times 7$ fine cells. The reservoir is originally saturated with oil; water is injected to displace oil. We inject water from the upper left corner and produce in the lower right corner. The initial reservoir pressure is 2000 psi. The water injection rate is constant at reservoir conditions (50 bbl/day) and the reservoir fluid is produced at the same rate. The injection and production rates are evenly distributed in the coarse cells (e.g. injection in the left upper coarse cell and production in the right lower coarse cell). Figs. 4–7 depict the pressure and saturation at $t = 0.2$ PVI and $t = 0.8$ PVI(pore volume injected), respectively, computed by three different methods: (1) the fine-scale method (*FM*), (2) the multiscale method without adaptivity of the transport computation (Schwartz-overlap for transport, *MSOM*), and (3) the multiscale method with adaptive transport computation (*MSAT*) proposed in this paper. The differences in pressure and saturation computed by the three methods in Figs. 4–7 are quite small.

In Fig. 8 the saturations, adaptively computed by *MSAT*, are shown for three different times. The white squares indicate Region 2, in which Prolongation Operator I (Schwartz-overlap) is employed, at least once, in the iteration of pressure and saturation calculations for the specific time step. Since the transport equation is nonlinear in saturation, multiple Newton iterations are usually required. So, for a given time step, the prolongation operator can be switched from I to II during the iterative process, if the saturation change becomes smaller than the transition criterion. The black squares in Fig. 8(a) indicate Region 3, where Prolongation Operator II was used at least once during the time step. Note that Prolongation Operator I is used mainly in the region around the sharp saturation front. Furthermore, Prolongation Operator II was employed if saturation and total-velocity changes were small. Later in time, as the saturation distribution became well established in most of the domain, Prolongation Operator III was widely employed in transport calculation. Note that determination of the Regions is done automatically and adaptively by the simulator based on the computed transition criteria during the solution process.

In Table 1 the $L_2$ norms of *MSOM* and *MSAT* solutions, with respect to the reference solution (*FM*), are tabulated for various time steps, and the adaptivity ratios in pressure and saturation calculations are also included. The $f_p$ denotes the fraction of updated basis functions, $f_{\mathrm{I}}$ the fraction of coarse blocks that need fine-scale transport calculation by Prolongation Operator I, $f_{\mathrm{II}}$ is the fraction of coarse blocks that employ Prolongation Operator II. All the adaptivity statistics are expressed as the average fraction computed from the initial condition up to the current time step. For instance, the fraction of coarse cells, in which Prolongation Operator I was applied to compute the saturation field from $t = 0$ to $t = 0.8$ PVI was 6.01%.

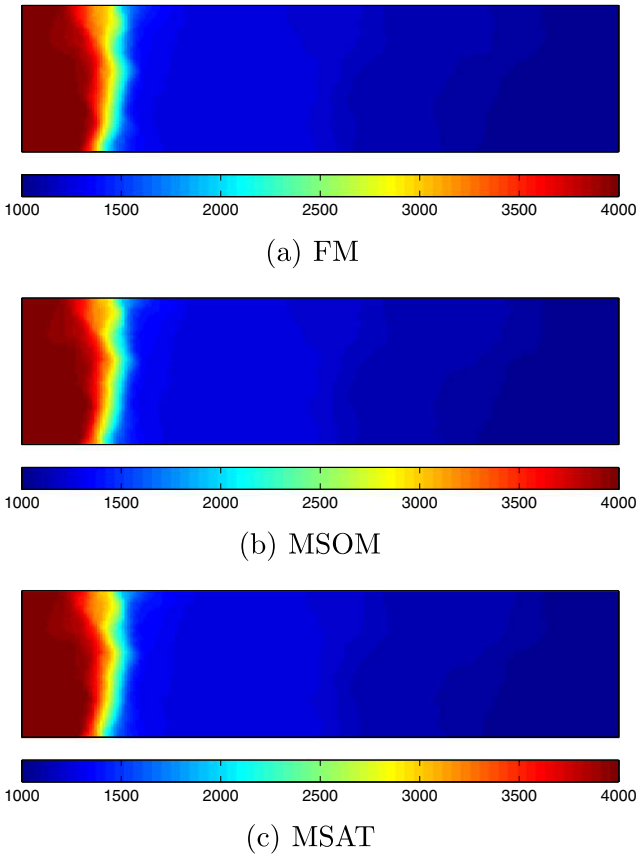


**Fig. 20.** Pressure distribution at $t = 4\tau_o$ in Case 3 with Dirichlet boundary condition.

From this numerical example, we first note that pressure from the adaptive transport calculation of this paper (*MSAT*) is as accurate as that from the original MSFV [18] without transport calculation adaptivity (*MSOM*). *MSAT* yields slightly higher numerical errors in saturation computation than *MSOM*, but these errors are quite small. Numerical errors in cumulative oil recovery and oil fraction in production curves are barely noticeable in Fig. 9. Secondly, the basis function updates for pressure calculation continuously decrease as the front moves from the injection well to the production well. As the total-mobility change is, in general, smaller than the saturation change, the pressure changes during the displacement process are rather small. As a result, a small percentage of basis functions is required to be updated (e.g. 1.95% in 1.5 PVI). Similarly, while the total-velocity can be a strong function of location, it tends to change slowly in time, and for this example the velocity updating during this long injection period of 1.5 PVI is only 3.44%. By comparison, the saturation front experiences a large transition region as it moves from the injection well to the production well. The fraction of the coarse-grid model that requires the original fine-scale transport calculation varies between 4.55% and 26.00%. Obviously, we could consider increasing the adaptivity by relaxing the transition criteria ($\Delta_1$ and $\Delta_2$), but this is likely to lead to less accurate results.

### 6.2. Case 2: Mildly heterogeneous domain

In this second example, we consider a reservoir model with heterogeneous permeability field with moderate correlation lengths. We employ the same setting as in the previous case, except that the permeability field is log-normal with a mean of logarithmic permeability of 4 and a variance of 2. The dimensionless isotropic spatial correlation length is 0.2. The permeability is generated by the Sequential Gaussian Simulation Method [10], and the resulting permeability field is depicted in Fig. 10.

In Figs. 11–14, the pressure and saturation distributions at $t = 0.2$ and $t = 0.8$ PVI are respectively compared for three different methods, *FM*, *MSOM* and *MSAT*. In the presence of highly varying and correlated permeability field, the water saturation distribution exhibits a complex structure as demonstrated in Fig. 14, which contrasts with the simple, symmetric saturation distribution of the previous case in Fig. 7. Note the excellent accuracy of the numerical results from the multiscale methods of *MSOM* and *MSAT*. The largest saturation errors are localized in the regions where the permeability is very low.

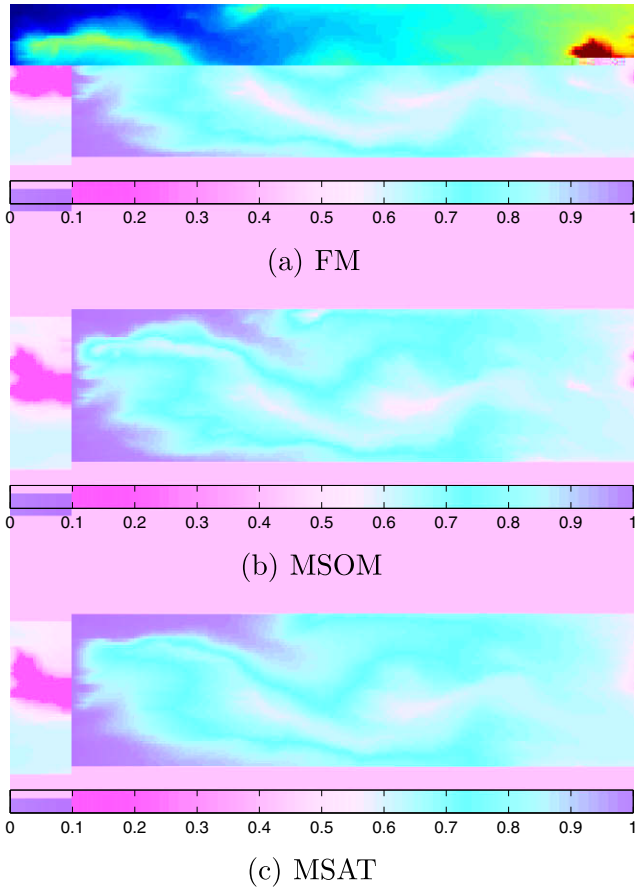


**Fig. 21.** Saturation distribution at $t = 4\tau_o$ in Case 3 with Dirichlet boundary condition.

Furthermore, adaptive saturation calculation of *MSAT* yields numerical results that are quite close to the original multiscale method without adaptive transport (*MSOM*) [18]. In Table 2, $L_2$ norms of *MSOM* and *MSAT*, with respect to the reference solution (*FM*), are tabulated for various time steps, and the adaptivity ratios in pressure and saturation calculations are also presented. As shown in Figs. 15, the adaptivity of saturation computation is similar to that for the homogeneous case. Prolongation Operator I is employed mainly around steep saturation gradients, and Prolongation Operator II is then used until the saturation distribution becomes established.

The cumulative oil recovery and the produced oil fraction are plotted in Fig. 16. The production histories of the multiscale methods (*MSOM* and *MSAT*) are hardly distinguishable from the fine-scale reference solution (*FM*). This numerical example with log-normal permeability clearly demonstrates that the adaptive transport algorithm is highly efficient and quite accurate.

### 6.3. Case 3: Highly heterogeneous model

The permeability field is adapted from the top layer of the SPE 10 Problem [8] with a fine-grid of $220 \times 54$. A $20 \times 6$ coarse-grid (i.e., a coarsening factor of $11 \times 9$) is imposed. The log- permeability field is shown in Fig. 17. The initial pressure is 4000 psi. The left boundary is kept at a constant pressure of 4000 psi with water injection, and the right boundary is kept at a constant pressure of 1000 psi with reservoir fluid production. As the production and injection rates are continuously changing with time, we define a characteristic time

$$\tau_o = \frac{\phi L_x^2 \bar{\mu}}{\bar{k}|p^{left} - p^{right}|}, \tag{53}$$

where $\bar{\mu}$ and $\bar{k}$ denote characteristic viscosity and permeability, respectively, and $L_x$ is the model dimension in $x$-direction. The arithmetic average of water and oil viscosity is chosen as $\bar{\mu}$ and the geometric average of permeability as $\bar{k}$.

The pressure and saturation distributions at $t = \tau_o$ and $t = 4\tau_o$ from the reference solution and multiscale methods are depicted in Figs. 18–21, respectively. Even though the model contains a highly heterogeneous permeability field, the pressure field in Figs. 18 and 20 exhibits a simple profile along the flow direction due to the Dirichlet boundary conditions and a

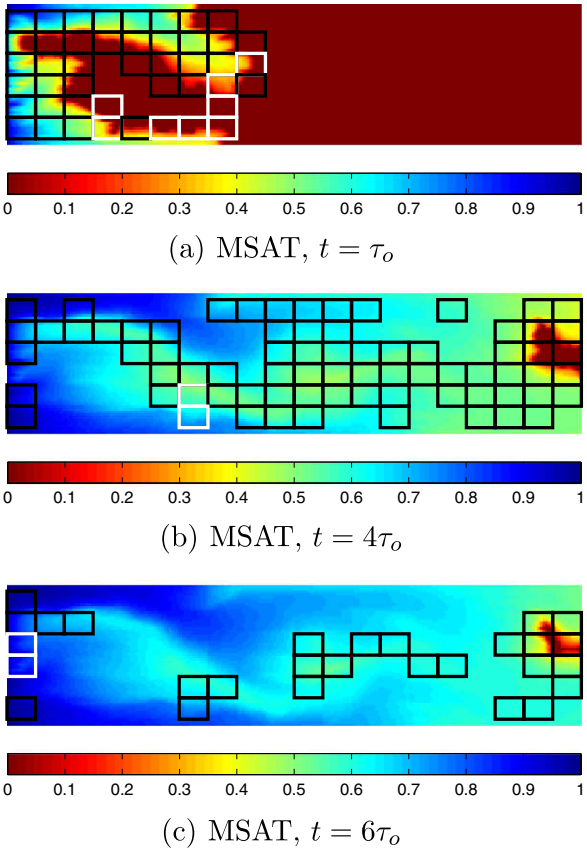


**Fig. 22.** Adaptive saturation computation for three time steps in Case 3: the white and black squares, respectively, denote the region where Prolongation Operator I and II was applied, respectively, at least once, in iterative saturation calculation for this time step.

much larger domain length compared to its width. On the other hand, the saturation distribution clearly indicates that the underlying distribution of heterogeneity results in a complex saturation field, as seen in Figs. 19 and 21. Prolongation Operator I was used in only a few regions, either around the saturation fronts or where the total-velocity changes significantly during the timestep, as shown in Fig. 22. This result is clearly shown in Table 3. The fraction of Operator I application is less than 5% in all the listed time steps; and in later times, Operator III is employed in most of the domain. The cumulative oil recovery and the oil fraction in production are plotted in Fig. 23. The fine-scale results and the multiscale results are in excellent agreement, in spite of the high degree of heterogeneity and the large correlation lengths. The results of the adaptive multiscale transport computations and the original multiscale method are nearly identical. Due to the strong heterogeneity, we observe slightly larger discrepancy between the fine-scale and multiscale results in this example. However, we believe that this level of accuracy is within the acceptable limits for engineering applications. In Table 3 $L_2$ norms of *MSOM* and *MSAT*, with respect to the reference solution (*FM*), are also tabulated for various times, and the adaptivity statistics in pressure and saturation calculation are also presented. Even in this highly heterogeneous problem, the adaptivity ratios of pressure and saturation are not much different from the previous examples. Since the saturation adaptivity requires Prolongation Operator I (expensive Schwartz-overlap method) only for 2–5% of the domain, the new algorithm (*MSAT*) is significantly more efficient than the original multiscale algorithm (*MSOM*).

### 6.4. Case 4: Three-dimensional models

In order to examine CPU improvement by the new adaptive transport algorithm (MSAT), we constructed two three-dimensional models with 97,200 cells ($45 \times 45 \times 48$) and 995,328 cells ($144 \times 144 \times 48$). Permeability fields are generated by a sequential Gaussian simulation method [10]. The logarithm of permeability has the Gaussian distributed histogram with

**Table 3**
Error norms and adaptivity statistics for Case 3: the variables are defined in the caption of Table 1.

| $t$ ($\tau_o$) | $e_p$ | | $e_s$ | | $f_p$(%) | | $f_{\mathrm{I}}$ (%) | $f_{\mathrm{II}}$ (%) |
|---|---|---|---|---|---|---|---|---|
| | MSOM | MSAT | MSOM | MSAT | MSOM | MSAT | MSAT | MSAT |
| 1 | 7.37e−3 | 7.88e−3 | 3.20e−2 | 3.87e−2 | 3.78 | 3.76 | 4.20 | 7.35 |
| 2 | 6.94e−3 | 7.90e−3 | 4.12e−2 | 5.07e−2 | 4.41 | 4.49 | 4.28 | 15.77 |
| 3 | 7.28e−3 | 7.85e−3 | 3.14e−2 | 4.20e−2 | 4.65 | 4.79 | 3.82 | 24.85 |
| 4 | 7.14e−3 | 7.59e−3 | 2.35e−2 | 3.54e−2 | 4.55 | 4.61 | 3.40 | 30.22 |
| 5 | 7.07e−3 | 7.26e−3 | 1.96e−2 | 3.19e−2 | 4.24 | 4.25 | 2.96 | 31.47 |
| 6 | 7.07e−3 | 7.14e−3 | 1.73e−2 | 2.99e−2 | 3.87 | 3.89 | 2.58 | 29.98 |

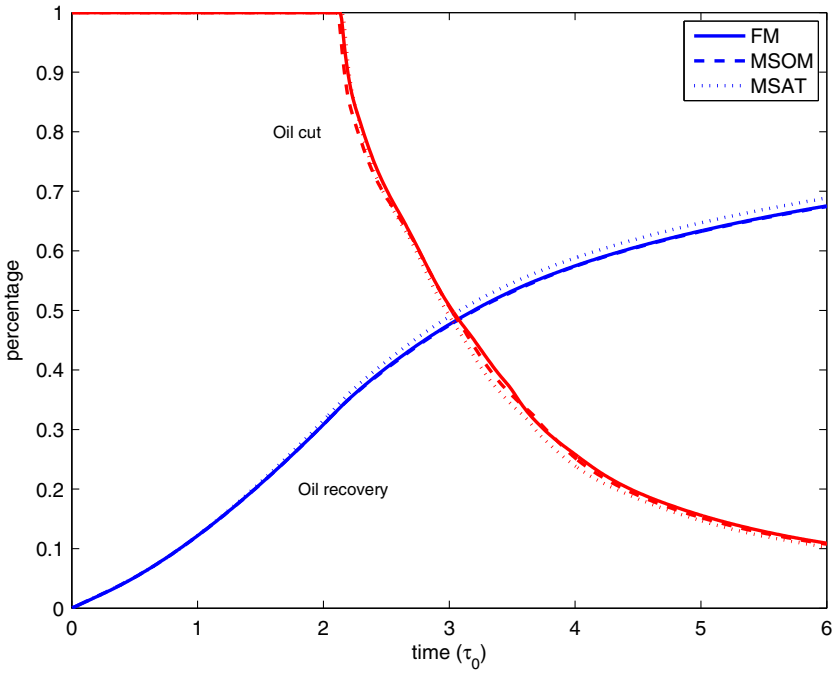


**Fig. 23.** Cumulative oil recovery and oil fraction in production (oil cut) in Case 3.

**Table 4**
CPU comparisons for 3-d models at $t = 0.6$ PVI.

| Number of cells | 97,200 | 995,328 |
|---|---|---|
| Fine-scale (*FM*) CPU (min) | 25.6 | 1618.7 |
| Original MS (*MSOM*) CPU (min) | 13.3 | 281 |
| Adaptive MS (*MSAT*) CPU (min) | 10.1 | 133 |

a mean of 50 md and standard deviation of 1.5. The same coarse-grid model of $9 \times 9 \times 6$ is used for these two models. The CPU times for 0.6 PVI are shown in Table 4.

For the small model with 97,200 cells, the original MSFV (MSOM) and the MSFV with adaptive transport algorithm (MSAT) reduced CPU by 48% and 61%, respectively, over the fine-grid simulation. Furthermore, for the large model with 995,328 cells, the CPU improvement becomes very significant; 83% CPU reduction by MSOM and 92% CPU reduction by MSAT. The numerical efficiency improvements by MSFV are naturally problem-dependent. As the model size becomes large, we expect MSOM and MSAT to speed up simulation runs drastically. We also note that for the large 3-d model MSFV with adaptive transport algorithm can improve numerical efficiency by a factor of two or more over the original MSFV.

## 7. Concluding remarks

The focus of this paper was the development of a multiscale finite-volume (MSFV) method for solving the nonlinear multiphase transport problem (i.e., saturation equations). A two-level algebraic framework, with appropriate definition of the prolongation and restriction operators, is used to describe the multiscale treatment of both flow and transport. The prolongation and restriction operators for the pressure, which rely on basis functions computed on a dual coarse grid, proposed by Jenny et al. [18] are used here. The transport equations for saturation are nonlinear and hyperbolic; as a result, coarsening and interpolation operators for saturation cannot, in general, be formulated via generic basis functions as for the pressure equation. We propose a conservative restriction operator and three adaptive prolongation operators to deal with the saturation field. For the timestep under consideration, different prolongation operators are used based on the region that the particular coarse cell belongs to. Specifically, we divide the coarse-grid into three regions: (1) Region 1 where the injection fluid has not yet invaded the cell, (2) Region 2 where an injection front encroached and the saturation of the injection fluid increases rapidly, and (3) Region 3 where the saturation changes slowly after the sharp front has moved through. A criterion to identify the transition between the various regions is proposed. In Region 1, the transport computations can be completely skipped; whereas in Regions 2 the local fine-scale transport equations are solved iteratively using a coarse-grid (Prolongation Operator I). Finally in Regions 3, we developed two efficient approximate prolongation operators: Prolongation Operator II that reconstructs the fine-scale velocity and is locally conservative on the fine-grid, and Prolongation Operator III, which interpolates saturation changes to yield a locally conservative scheme, but only on the coarse-grid. We observed that Prolongation Operators II and III provide very accurate numerical results for the test problems, except for local regions around saturation fronts.

The new method was tested using various models with homogeneous and heterogeneous permeabilities. It was clearly demonstrated that the multiscale results with adaptive transport calculations are in excellent agreement with the fine-scale solutions. Furthermore, the adaptivity of flow and transport equations in the MSFV of this paper are more computationally efficient compared with the original MSFV approach, which is already significantly more efficient than conventional fine-scale strategies. The current algorithm has been tested for two- and three-dimensional, incompressible two-phase flow without gravity and capillary pressure. We are working on extending the implementation to three-dimensional domains and incorporating compressibility, gravity, and capillary forces.

## Acknowledgment

This work has been supported in part by Chevron Energy Technology Company and Chevron/Schlumberger Intersect Alliance Technology. Financial support was also provided by the Reservoir Simulation Industrial Affiliates Program (SUPRI-B) at Stanford University.

## References

[1] J.E. Aarnes, Y. Efendiev, An adaptive multiscale method for simulation of fluid flow in hetrogeneous media, Multiscale Model. Simul. 5 (3) (2006) 918–939.
[2] T. Arbogast, Implementation of a locally conservative numerical subgrid upscaling scheme for two-phase darcy flow, Comput. Geosci. 6 (2002) 453–481.
[3] T. Arbogast, S.L. Bryant, A two-scale numerical subgrid technique for waterflood simulations, SPEJ (2002) 446–457. Dec..
[4] J.W. Barker, S. Thibeau, A critical review of the use of pseudo-relative permeabilities for upscaling, SPE Res. Eng. (1997) 138–143.
[5] W.L. Briggs, V.E. Henseon, S.F. McCormick, A multigrid tutorial, SIAM (2000).
[6] Y. Chen, L.J. Durlofsky, M. Gerritsen, X.H. Wen, A coupled local-global upscaling approach for simulating flow in highly heterogeneous formations, Adv. Water Resour. 26 (2003) 1041–1060.
[7] Z. Chen, T.Y. Hou, A mixed finite element method for elliptic problems with rapidly oscillating coefficients, Math. Comput. 72 (2002) 541–576.

[8] M.A. Christie, M.J. Blunt, Tenth spe comparative solution project: a comparison of upscaling techniques, SPERE 4 (4) (2001) 308–317.
[9] G. Dagan, Flow and Transport in Porous Formations, Springer-Verlag, New York, 1989.
[10] C.V. Deutsch, A.G. Journel, GSLIB: Geostatistical Software Library and User's Guide, Oxford University Press, New York, 1998.
[11] Y. Efendiev, L.J. Durlofsky, Numerical modeling of subgrid heterogeneity in two phase flow simulations, Water Resour. Res. 38 (2002), doi:10.1029/2000/WR000190.
[12] Y. Efendiev, L.J. Durlofsky, S.H. Lee, Modeling of subgrid effects in coarse-scale simulations of transport in heterogeneous porous media, Water Resour. Res. 36 (2000) 2031–2041.
[13] H. Hajibeygi, G. Bonfigli, M.A. Hesse, P. Jenny, Iterative multiscale finite-volume method, J. Comp. Phys. 227 (19) (2008) 8604–8621.
[14] T. Hou, X.H. Wu, A multiscale finite element method for elliptic problems in composite materials and porous media, J. Comp. Phys. 134 (1997) 169–189.
[15] T.Y. Hou, A. Westhead, D. Yang, A framework for modeling subgrid effects for two-phase flows in porous media, Multiscale Model. Simul. 5 (4) (2006) 1087–1127.
[16] P. Jenny, S.H. Lee, H.A. Tchelepi, Multi-scale finite-volume method for elliptic problems in subsurface flow simulation, J. Comp. Phys. 187 (2003) 47–67.
[17] P. Jenny, S.H. Lee, H.A. Tchelepi, Adaptive multiscale finite volume method for multi-phase flow and transport, Multiscale Model. Simul. 3 (2004) 50–64.
[18] P. Jenny, S.H. Lee, H.A. Tchelepi, An adaptive fully implicit multi-scale finite-volume algorithm for multi-phase flow in porous media, J. Comp. Phys. 217 (2006) 627–641.
[19] S.H. Lee, C. Wolfsteiner, H.A. Tchelepi, A multiscale finite-volume method for multiphase flow in porous media: black oil formulation of compressible, three phase flow with gravity and capillary force, Comp. Geosci. 12 (2008) 351–366.
[20] R. LeVeque, Numerical Methods for Conservation Laws, Birkhäuser, 1992.
[21] I. Lunati, P. Jenny, Multi-scale finite-volume method for compressible multi-phase flow in porous media, J. Comp. Phys. 12 (2006) 337–350.
[22] I. Lunati, P. Jenny, Multi-scale finite-volume method for multi-phase flow with gravity, Comp. Geosci. 217 (2008) 627–641.
[23] H.A. Tchelepi, P. Jenny, S.H. Lee, C. Wolfsteiner, Adaptive multiscale finite volume framework for reservoir simulation, SPEJ 12 (2007) 188–195.
[24] H. Zhou, H.A. Tchelepi, Operator based multiscale method for compressible flow, SPEJ 13 (2008) 267–273.